ELSEVIER

Coordination Chemistry Reviews
200–202 (2000) 595–632

COORDINATION CHEMISTRY REVIEWS

www.elsevier.com/locate/ccr

Electronic structures of active sites in electron transfer metalloproteins: contributions to reactivity

Edward I. Solomon *, David W. Randall, Thorsten Glaser

Department of Chemistry, Stanford University, Stanford, CA 94305 USA

Received 18 November 1999; received in revised form 24 February 2000; accepted 24 February 2000

Contents

Abstract

Many electron transfer centers in biology involve metal complexes, that exhibit unique spectral features. These reflect highly covalent electronic structures, which contribute to the electron transfer function of the protein. The blue copper center has a highly covalent copper–thiolate bond, which promotes long range electron transfer. The Cu_A center is a mixed valence binuclear complex that is completely delocalized even in low symmetry protein

* Corresponding author. Tel.: +1-650-7239104; fax: +1-650-7250259.
E-mail address: edward.solomon@stanford.edu (E.I. Solomon).

PII: S0010-8545(00)00332-5

environments. The [2Fe–2S] center is valence localized in the mixed valence Fe(III)Fe(II) oxidation state, while the mixed valence [2Fe–2S] sub-sites in [4Fe–4S] clusters are completely valence delocalized. Factors which contribute to electron localization/delocalization in these mixed valence sites are experimentally evaluated using a variety of spectroscopic and electronic structural methods. These include the very powerful technique of ligand K-edge X-ray absorption spectroscopy for determining the covalency of ligand–metal bonds.

Keywords: Electron transfer; Copper proteins; Iron–sulfur clusters; Mixed valence compounds; Double exchange; Ligand K-edge X-ray absorption spectroscopy

1. Introduction

Electron transfer (ET) is an integral component in a diverse range of important biological functions including photosynthesis, respiration, and nitrogen fixation. Biological ET can involve transferring electrons between proteins (interprotein ET) [1] or between redox centers within a protein (intraprotein ET) [2]. Summarized in Fig. 1 are representative active sites of several classes of ET metalloproteins. The mononuclear blue Cu center found in the plastocyanins and azurins has a Cu ion in a trigonally distorted tetrahedral environment [3–5]. The trigonal plane contains a CysS ligand with a very short ca. 2.1 Å S–Cu(II) bond and two HisN ligands exhibiting bond lengths of ca. 1.9 Å and are in the normal range of N–Cu(II) bonds. The axial ligand is usually a MetS with an exceptionally long ca. 2.9 Å Cu–S

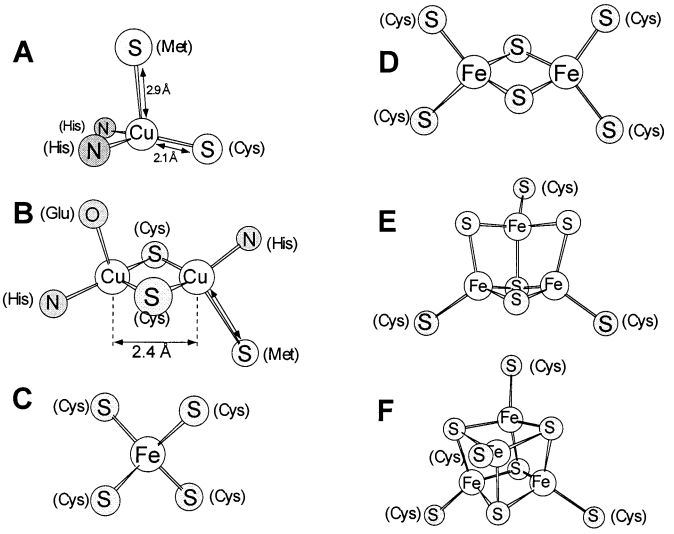

Fig. 1. Cu and FeS electron transfer centers. (A) mononuclear blue Cu center, (B) binuclear Cu_A center, (C) mononuclear rubredoxin center, (D) binuclear [2Fe–2S] ferredoxin, (E) trinuclear [3Fe–4S] ferredoxin, (F) tetranuclear [4Fe–4S] ferredoxin (or HiPIP).

bond. Several perturbed blue Cu centers exist in which the axial MetS–Cu bond is shorter and the geometry is distorted, or where this ligand is substituted. The binuclear Cu_A site [6] found in cytochrome *c* oxidase (COX) and nitrous oxide reductase is a completely delocalized mixed valence binuclear center [7,8] (class III mixed valence in the Robin and Day scheme [9]) in its oxidized state with two $Cu^{1.5+}$ separated by ca. 2.4 Å [10,11] and bridged by two CysS [12–16]. Again the Cu sites are in an approximately trigonal coordination environment with the third ligand in the equatorial plane being a HisN. The axial ligand on one Cu is MetS and on the second Cu is a carbonyl oxygen of a backbone amide (the side-chain is Glu in COX). Important questions for this site have been whether a Cu–Cu bond is present and how this site remains delocalized in low-symmetry protein environments.

Common iron sulfur (Fe–S) centers [6,17–20] involved in ET have either one Fe with four CysS ligands in a distorted tetrahedral environment (rubredoxin), or two, three, or four Fe clusters (ferredoxins and high potential iron proteins–HiPIPs) with μ_2 and/or μ_3 sulfide bridges and CysS ligands to complete the tetrahedral Fe coordination sphere. The iron–sulfur bond lengths in the Fe–S clusters show considerable variation; there is a large distribution for each site and among the Fe–S clusters from different organisms. The Fe–cysteine bond length ranges are: 2.2–2.3 Å in rubredoxins, 2.3–2.4 Å in [2Fe–2S], and 2.2–2.3 Å in [4Fe–4S]; whereas the bond lengths to the bridging sulfides are 2.1 Å in [2Fe–2S] and 2.2–2.3 Å in [4Fe–4S]. The distance between two iron centers is 2.70 Å in both the dimers and tetramers; there is a slight variation in the Fe–Fe distance in [4Fe–4S] clusters depending on the oxidation state [21]. In the binuclear iron–sulfur clusters the two iron centers are antiferromagnetically coupled [22–27] in both redox forms: the homovalent oxidized (Fe(III)Fe(III)) and the mixed valence reduced (Fe(III)Fe(II)) states. In the mixed valence form of the dimeric clusters the extra electron is localized on one iron center [24] (class II mixed valence [9]). In contrast, in the trinuclear and tetranuclear iron–sulfur clusters the excess electron in the mixed valence forms is delocalized over a pair of two iron centers (class III mixed valence [9]). This delocalization leads to a net ferromagnetic interaction between the two iron ions via a double exchange mechanism (vide infra) [28,29]. Finally, the most common heme ET centers are cytochromes *b* and *c*. In the former, protoporphyrin IX is non-covalently linked to the protein, while in the latter this heme prosthetic group is covalently bound to the protein through thioether linkages. There are different axial ligands in the different cytochromes, the most common being HisN/MetS in cytochrome *c* and two HisN in cytochrome *b* [30]. Good reviews exist for heme ET sites [31–36]. Here we focus on the electronic structures of the Cu and Fe–S ET sites and their effects on reactivity.

Electronic structure contributes to the reactivity of ET sites through its effects on the thermodynamics (i.e. reduction potentials, E^0) and kinetics (k_{ET}) of ET. The potentials will have contributions from both the protein environment (dielectric, dipole orientation, H-bonds, etc. [37–46]) and the ionization energy of the active site. The latter is determined by the active site electronic structure and specifically the nature and geometric orientation of the ligand–metal and metal–metal bonds.

These interactions can affect the effective nuclear charge on the metal ion, the energy of the redox active valence orbital and electronic relaxation, all making significant contributions to E^0 [38]. According to Marcus theory [47], the semi-classical rate of long range ET contains three terms: (1) $\Delta G^{\dagger}$, the thermodynamic driving force, which depends on the difference in the reduction potentials (E^0) of the electron acceptor and donor; (2) the through protein electronic coupling between the donor and acceptor (H_{DA}); and (3) the reorganization energy associated with the active site geometry change (λ_{inner}) and reorientation of the solvent dipoles (λ_{outer}, where $\lambda = \lambda_{inner} + \lambda_{outer}$) with redox. Marcus and co-workers determined the functional dependence of these influences [47]:

$$k_{ET} = \sqrt{\frac{\pi}{(h/2\pi)^2 \lambda k_B T}} \cdot (H_{DA})^2 \cdot \exp\left[-\frac{(\Delta G^{\dagger} + \lambda)^2}{4\lambda k_B T} \right] \quad (1)$$

Here $k_B T$ represents the thermal energy. The exponential in this equation is maximized when $(\Delta G^{\dagger} + \lambda)$ is minimized. Since the thermodynamic driving force ($\Delta G^{\dagger}$) for many biological ET processes is relatively small, it is important that the reorganization energy (λ) be small as well. In fact, all the ET sites in Fig. 1 show little geometry change upon oxidation and therefore have low Frank–Condon barriers to ET. In some cases (e.g. the blue Cu center), the high anisotropic covalency of a specific ligand–metal bond provides very efficient electronic coupling (H_{DA}) for long range ET [48]. In all cases, the ligation and environment tune the potentials to function in the appropriate physiological range.

These ET active sites are all known to exhibit unique spectral features. These reflect novel electronic structures that can make significant contributions to reactivity [49]. The blue Cu sites generally show a very small parallel hyperfine splitting in the EPR spectrum and intense CysS $\pi \rightarrow$ HOMO charge transfer (CT) transition in the absorption spectrum [50]. Both reflect high anisotropic covalency of the thiolate–Cu bond (vide infra). The oxidized Cu_A center has an EPR signal with equal hyperfine coupling to both Cu centers [7,8,51] (class III delocalized [9]). This center exhibits intense absorption bands at ca. 800 nm and two bands centered at 500 nm, the former is the $\psi \rightarrow \psi^*$ transition of the metal–metal bond and the latter are CysS $\rightarrow$ Cu CT transitions that reflect the orientation of the redox active orbital (vide infra) [52,53]. The iron–sulfur centers have intense absorption features due to sulfur ligation [18], which make them difficult to study by traditional spectroscopic methods and EPR properties which in the monomer reflect a highly covalent thiolate–Fe(III) bond [54]. In the multinuclear Fe–S clusters these spectral features reflect interactions between the irons due to a competition between super-exchange and double-exchange [26,27]. Finally, for the cytochromes, the ground state properties are dominated by the large splitting of the dπ orbitals [55–57], and the absorption spectra are dominated by intense $\pi \rightarrow \pi^*$ and Fe–porphyrin CT transitions [32,58], where the latter reflects high delocalization of the d orbitals onto the porphyrin ligand.

Using a multifaceted spectroscopic approach augmented by electronic structure calculations, an understanding of the unique electronic structures of the metalloprotein active sites in Fig. 1 has been developed, that provides insight into

electronic structure contributions to their ET properties. Furthermore, there has been of significant interest in the possible role of the protein in determining the geometric and electronic structure of these active sites. This relates to the concept of the entatic [59] or rack-induced [60] state in bioinorganic chemistry, where it has been proposed that the protein environment can place constraints on the active site complex to activate it for reactivity. Note that some controversy exists in the usage of these two terms [59,61,62]. Here we review the present understanding of the electronic structure contributions to ET reactivity (E^0 and k_{ET}) and the role of the protein in affecting active site geometric and electronic structure. The following topics in metalloprotein ET are considered: (1) the electronic structures of perturbed blue Cu centers and the role of the protein in determining their geometric structure in relation to 'classic' blue Cu proteins like plastocyanin and azurin; (2) the contributions of direct metal–metal bonding and superexchange to the electronic structure of the Cu_A centers and their contributions to reactivity; (3) the origin of electron localization in the mixed valence two Fe ferredoxins in contrast to the delocalization in a binuclear $Fe(2.5)^+Fe(2.5)^+$ reference compound; and (4) the use of sulfur K-edge X-ray absorption spectroscopy (XAS) to elucidate the electronic structures of the one, two, and four Fe–S centers to determine the origin of delocalization in the mixed valence four iron centers compared to localization in the mixed valence two iron centers.

2. Mononuclear Cu ET centers

2.1. Classic blue copper sites

The unique spectral features of the classic blue copper sites in plastocyanin and azurin have been shown to reflect a novel electronic structure that plays a key role in the long range electron transfer properties of these proteins. These have been reviewed in Ref. [50] and are only briefly summarized here. As shown in Fig. 1(A), the prototypical blue Cu protein, plastocyanin, has a ca. C_{3v}-distorted tetrahedral rather than the tetragonal geometry usually observed for Cu(II) complexes (due to the Jahn–Teller effect). The site is characterized by a short thiolate bond (CysS–Cu ca. 2.1 Å) and a long thioether bond (MetS–Cu ca. 2.9 Å) [63]. Associated with this unusual geometric structure is an inverted charge transfer spectrum with a low-energy, intense cysteine $S\pi \rightarrow Cu\ x^2 - y^2$ (axes defined in Fig. 6) transition and a high energy, weak $CysS\sigma \rightarrow Cu\ x^2 - y^2$ transition (Fig. 2) [50,64], as well as a very small parallel hyperfine splitting ($A_{\|}$) in the EPR spectrum ($< 90 \times 10^{-4}\ cm^{-1}$) [65]. These should be compared to the spectral features of normal tetragonal Cu(II) complexes ([Cu(tetb)(o-$SC_6H_4CO_2$)] with tetb = *rac*-5,7,7,12,14,14-hexamethyl-1,4,8,11-tetraazocyclotetradecane, as an example [66]) where the higher energy thiolate σ-Cu(II) charge transfer transition is intense and the lower energy charge transfer transition is weak (Fig. 2), and the value of $A_{\|}$ is much larger ($> 150 \times 10^{-4}\ cm^{-1}$).

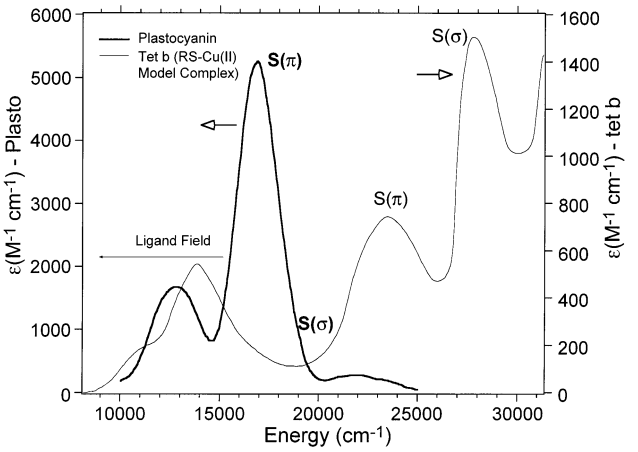

Fig. 2. Comparison of the absorption spectrum of the blue copper site in plastocyanin (thick trace) to the normal Cu(II)–thiolate model complex tetb (thin trace, from Ref. [66]) showing the inverted π/σ CT intensity pattern of plastocyanin.

The unique spectral features of the blue copper site derive from the highly covalent nature and orientation of the thiolate–Cu bond. The inverted π/σ intensity pattern demonstrates that the half-occupied x^2-y^2 HOMO of the oxidized site has significant overlap with the Sπ MO (perpendicular to the Cu–S–C plane) and little overlap with the Sσ MO (in the Cu–S–C plane). This experimentally demonstrates that the x^2-y^2 HOMO is oriented such that its lobes are bisected by the CysS–Cu bond [50], consistent with the results derived from electronic structure calculations [67–71]. The covalency of this interaction can be directly evaluated through sulfur K-edge X-ray absorption spectroscopy (XAS) (Fig. 3(A)) [72], where the intensity of the sulfur K pre-edge feature at ca. 2470 eV (a S $1s \rightarrow 3p$ electronic transition) reflects the amount of S 3p character in the half-occupied Cu x^2-y^2 orbital. The blue copper site has a very intense pre-edge feature relative to that of the tetb model complex, which has a normal thiolate–Cu(II) bond at 2.36 Å [66]. This experiment quantifies the Cys Sπ character in the Cu(II) x^2-y^2 orbital at 38% [73]. The complementary Cu L-edge XAS experiment (Fig. 3(B)) probes the Cu d character in the HOMO through the analysis of the Cu $2p \rightarrow 3d$ transition intensity at ca. 930 eV. This experiment also points to a highly covalent site since less intense Cu d character is observed in the HOMO of plastocyanin (42%) relative to that of normal tetragonal Cu complexes (ca. 60–70%) [74].

The covalency of the blue Cu site quantified in these experiments provides strong electronic coupling (H_{DA}) into protein pathways for rapid long-range ET. Newton has shown the electronic coupling depends on α_L, which is the wavefunction coefficient of the ligand orbital in the redox active orbital $\psi^*_{HOMO} = \sqrt{1-\alpha^2}|\text{metal}\rangle - \alpha|\text{ligand}\rangle$ [75,76] and a function which depends upon the remainder of the donor–acceptor bridge, denoted here as $f(r_{DA})$:

$$H_{DA} \propto \alpha_L f(r_{DA}) \tag{2}$$

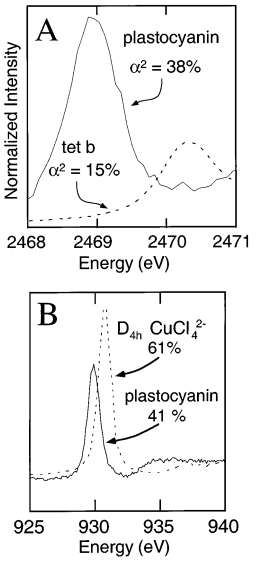

Fig. 3. XAS of plastocyanin at different energies. (A) S K-edge compared to tetb model complex and (B) Cu L-edge compared to $[CuCl_4]^{2-}$.

The exact form of $f(r_{DA})$ depends on the model used for long range electron transfer, i.e. through bond or through space pathways, etc. [77–80]. Since the ET rate, k_{ET}, depends quadratically on H_{DA} [47], the large anisotropic CysS covalency

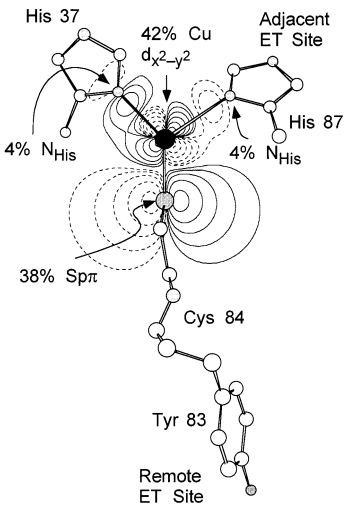

Fig. 4. Redox active orbital in plastocyanin showing the large anisotropic covalency of the Cu thiolate π interaction that activates the remote site (ca. 13 Å from the blue copper center) for electron transfer. The half-occupied HOMO is oriented with the x^2-y^2 orbital in the $(Cu)(HisN)_2CysS$ plane and the MetS is approximately perpendicular to this plane and along the z-axis.

experimentally observed in the blue Cu center can dramatically affect ET rates [48]. As shown in Fig. 4 the large covalent interaction of the Cu x^2-y^2 orbital with the thiolate π orbital produces a very efficient hole super-exchange mechanism [81] for rapid ET through the Cys-Tyr pathway in plastocyanin (or a Cys-His pathway in the multicopper oxidases and nitrite reductases) to a remote acceptor site ca. 13 Å from the blue Cu center.

Photoelectron spectroscopic (PES) studies on reduced d^{10} blue copper relevant sites probing unconstrained Cu–ligand interactions [82] have indicated that the long thioether S–Cu(I) bond is imposed on the blue copper active site by the protein (2.9 versus 2.3 Å for a normal thioether–Cu(I) bond). In fact, a search of high quality structures ($R = 10\%$) in the Cambridge Structural Database [83] reveals that an average thioether–Cu(I) bond is ca. 2.32 ± 0.14 Å in predominantly four coordinate complexes with N_2S_2 or S_4 ligation (Fig. 5). The long MetS–Cu distance in the blue Cu active site would, therefore, implicate an entatic or rack-induced state for the reduced site, rather than the oxidized site as had generally been considered [59,60]. Querying the CSD for an average axial Cu(II)–thioether distance gives a value of 2.68 ± 0.16 Å, which is much closer to the 2.8 Å distance observed in the oxidized blue Cu site. The long thioether decreases its donor interaction with the copper, which is partially compensated by the short, strong Cys thiolate–Cu bond (Fig. 6(A)). This combination of geometric distortions removes the electronic degeneracy of the Cu xy and x^2-y^2 orbitals in the oxidized site and thus eliminates the Jahn–Teller distorting force (i.e. electronic–nuclear coupling

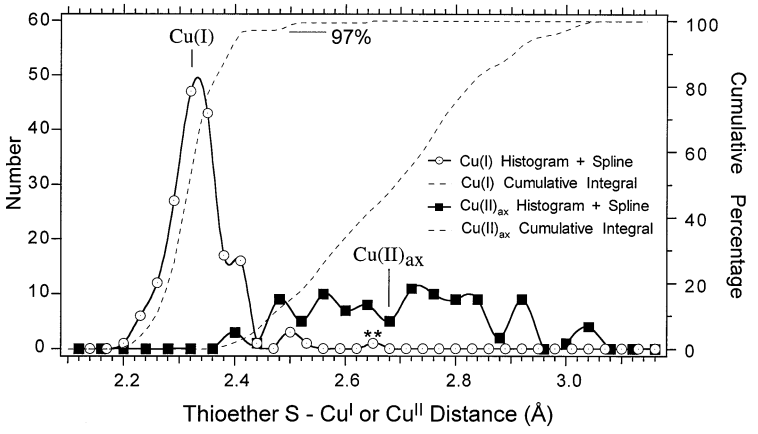

Fig. 5. Histogram of all Cu(I)–thioether and axial Cu(II)–thioether distances in model complexes in the Cambridge Structural Database [83]. The average thioether Cu(I)–S distance is 2.32 Å, while the average for Cu(II)–S(axial) is 2.68 Å; these averages are indicated on the graph. For Cu(I) the ligation spheres are N_2S_2 or S_4. Similar liganding atoms are in the Cu(II) ligation spheres. The solid lines are cubic spline fits of the histogram data and the dashed line is the cumulative integral, i.e. 97% of the Cu(I)–thioether distances are less than 2.45 Å. The one Cu(I) compound with R(Cu–S) ca. 2.6 Å (marked with **) involves a thioether fragment bridging two Cu centers [84].

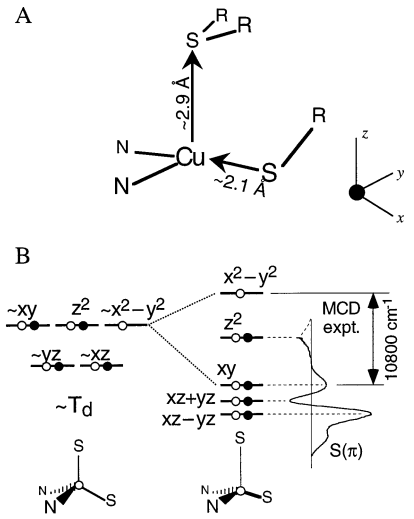

Fig. 6. Axial ligand effects on the electronic structure of blue Cu sites. (A) Thiolate charge donation compensates for decreased axial thioether donor interaction [85]. (B) Elimination of Jahn–Teller distortions in blue Cu sites: geometric distortion in (A) generates an electronic structure where x^2-y^2 and xy splitting is 10 800 cm^{-1} from low temperature MCD.

between these orbitals) that would typically be present in normal Cu(II) complexes and that leads to their tetragonal geometry [82]. A large ligand field splitting of these orbitals (ca. 10 800 cm^{-1}) is directly observed in the low-temperature MCD spectrum (Fig. 6(B)) [68,69,86]. This combination of long thioether and short thiolate bonds removes the Jahn–Teller force from the Cu(II) site and precludes a tetragonal distortion upon oxidation. The site, therefore, has a low reorganization energy (λ_{inner}) for ET, and it appears unnecessary for the protein to enforce the reduced geometry on the oxidized blue Cu center.

2.2. Perturbed blue Cu centers

The above description has lead to a coupled distortion model where the long thioether is associated with the short thiolate and together these eliminate the JT tetragonal distortion of the Cu site [69,87,88]. This coupled distortion model of the blue copper site is strongly supported by recent spectral studies on perturbed blue copper centers [87]. Proteins, such as cucumber basic protein (also called plantacyanin), *Achromobacter cycloclastes* nitrite reductase (NiR), and stellacyanin, exhibit perturbed spectral features relative to those of plastocyanin and azurin, including increased absorption spectral intensity at 450 nm at the expense of the 600 nm band and rhombic EPR spectra [89–92]. It is clear that stronger axial interactions are a critical distinguishing feature of the active sites of these proteins

relative to plastocyanin. Also, these proteins divide into two different classes. In one class the axial Met ligand is replaced by a stronger field ligand (e.g. Gln in stellacyanin [93] and the M121Q mutant of *Alcalagenes denitrificans* azurin [94]), which distorts the site by shifting the Cu out of the $HisN_2CysS$ plane to produce a more tetrahedral geometry. This is revealed by shifts in the ligand field transitions in the MCD spectrum to lower energy by ca. 1000 cm^{-1} relative to plastocyanin [87].

The second class has the same ligand set as plastocyanin and azurin (i.e. axial MetS) yet exhibits dramatic spectral changes, including a transition from a blue to a green protein solution, over the series: plastocyanin → cucumber basic protein → NiR [87]. As shown in Fig. 7(A), these spectral changes correspond to a decrease in the CysS $\pi \rightarrow$ Cu $x^2 - y^2$ and increase in the CysS $\sigma \rightarrow$ Cu $x^2 - y^2$ charge transfer transition intensities. This indicates that the half-occupied $x^2 - y^2$ orbital is rotating from a π to σ interaction with the thiolate ligand, which is also supported by density functional calculations (Fig. 7(B)) [87,95]. From low temperature MCD spectra (Fig. 7(C)) [87], we observe that this dramatic spectral change is associated with a shift in the ligand field transitions to higher energy corresponding to a tetragonal distortion (rather than a tetrahedral distortion, as has been proposed [96,97]) of the ligand field of the blue copper site in going to nitrite reductase. From the crystallographic results summarized in Fig. 7(D) and (E) [63,98,99], on going from plastocyanin to cucumber basic blue to nitrite reductase the thioether S–Cu bond decreases by 0.3 Å and the thiolate S–Cu bond increases by > 0.1 Å. The weakening of the thiolate–Cu interaction along this series is also quantified by decreases in the Cu–S(Cys) stretching frequency in the resonance Raman spectrum [100,101]. Further, the CysS–Cu–MetS plane rotates relative to the HisN–Cu–HisN plane in a Jahn–Teller type ca. $\varepsilon(u)$ distortion toward a more tetragonal geometry. The reduction potential along this series decreases form ca. 370 mV in plastocyanin to ca. 320 mV in cucumber basic protein to ca. 240 mV in NiR. This is consistent with the tetragonal geometric distortion across this series, though it is clear that other effects of the protein environment will also influence E^0. In summary, these perturbed blue copper sites with the same ligand set as plastocyanin demonstrate that the protein does indeed contribute to the geometry of the site through the effects of a coupled distortion in which a stronger axial MetS–Cu interaction produces a weaker Cys–S–Cu bond which together result in a tetragonal Jahn–Teller distortion of the site [87].

3. The mixed valence binuclear Cu_A center

The remaining class of copper containing ET sites is the binuclear Cu_A center [6], which uses the Cu(1.5)Cu(1.5)/Cu(I)Cu(I) redox couple and is found in both cytochrome *c* oxidase (COX) and nitrous oxide reductase (N_2OR) [102,103]. In the transmembrane COX protein system, the Cu_A center is involved in both inter- and intraprotein ET. Cu_A receives electrons from cytosol soluble cytochrome *c* and rapidly passes these to the heme *a* center, which then transfers electrons to the

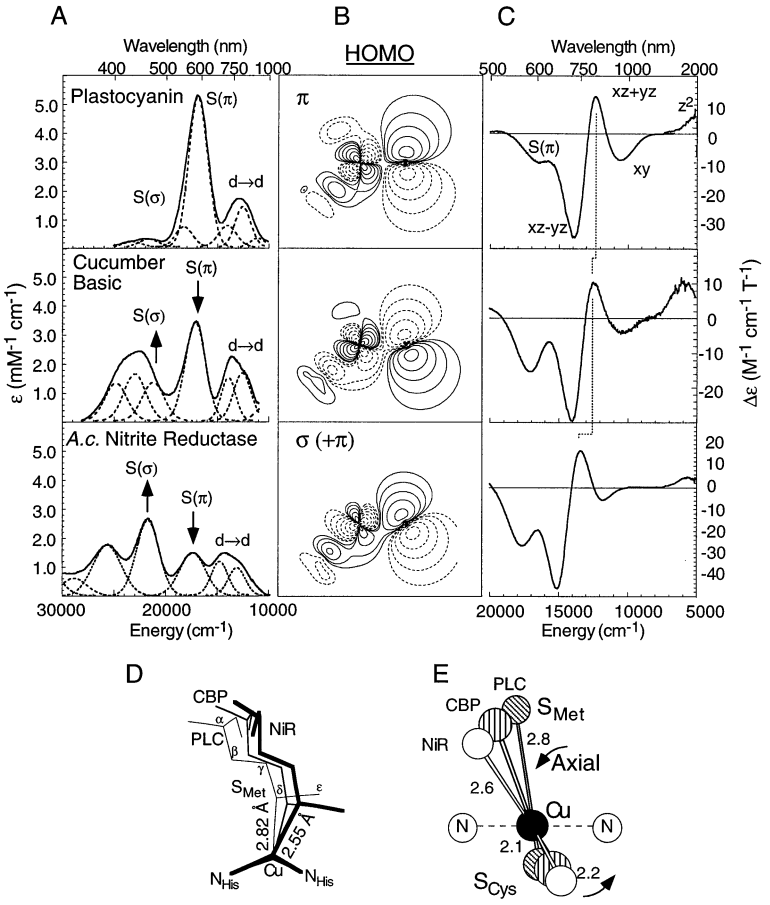

Fig. 7. Continuum of a coupled tetragonal distortion in a series of perturbed blue Cu proteins. (A) Low-temperature absorption spectra showing redistribution of spectral intensity in CysS π and σ CT bands. (B) Redox active orbitals calculated with Xα-SW showing rotation from π-type interaction in plastocyanin to σ (+ π) mixture in nitrite reductase. (C) MCD spectra showing a shift of the ligand field transitions to higher energy indicating a tetragonal distortion. (D) Crystal structures showing contraction of MetS-Cu bond associated with elongation of the CysS–Cu(II) bond and tetragonal $\varepsilon(u)$-like mode Jahn–Teller distortion (E).

catalytic heme a_3/Cu_B center where O_2 is reduced [104,105]. The Cu_A center in N_2OR is presumed to be involved in an analogous ET function, though the details are less well defined [103,106,107]. As shown in Fig. 1(B), the Cu_A center [12–16] contains a planar 'diamond core' containing two copper ions at a Cu–Cu distance of ca. 2.4 Å [10,11] bridged by two μ_2 S-Cys thiolates. EPR studies by Kroneck, Antholine and co-workers [7,8,51] first demonstrated that the oxidized site was completely delocalized by observing seven hyperfine-split resonances at $g_{\|}$, consistent with a dimer of $I = 3/2$ Cu nuclei. This delocalization is of key importance in Cu_A and significantly contributes to the redox properties of the site (vide infra) [52]. Here we focus on defining the contributions to electronic delocalization.

As shown in Fig. 8, the origin of electron delocalization in a mixed valence system is the bonding interaction (direct and indirect) between the valence d orbitals of the two copper ions. In Cu_A, only one set of Cu d orbitals is involved in this interaction, since all orbitals but one are completely occupied (i.e. the oxidized center has 19 electrons occupying the ten d orbitals of the two copper ions). In such a dimer, the valence d orbitals split into pairs with phases that are bonding and antibonding with respect to metal–metal interactions (whether or not such interactions are actually present) [108]. In oxidized Cu_A with one hole delocalized between the two centers an intense electronic transition, referred to as $\psi \rightarrow \psi^*$, can be observed from a filled MO to the higher energy partner of the dimer-split pair. From Fig. 8 the $\psi \rightarrow \psi^*$ transition energy gives an experimental value for the electronic coupling matrix element between the two Cu ions, $2H_{AB}$ [109,110], that is responsible for the electronic delocalization [111].

Two types of electronic interactions contribute to $2H_{AB}$: those involving the bridging ligands via an indirect superexchange pathway [112] and those involving direct metal orbital overlap via a metal–metal bond. The relative contributions of these two interactions to the Cu_A electronic structure have been evaluated through parallel spectral studies on the Cu_A site (from a soluble cytochrome *c* oxidase domain [113] or in the engineered blue Cu proteins *P.a.* azurin [114] and *T.v.* amicyanin [115]) and the mixed valence (MV) model complex of Tolman et al. [116]. The model system exhibits complete electron delocalization, but its Cu–Cu distance of 2.9 Å (Chart I) precludes a direct metal–metal bonding contribution to H_{AB}.

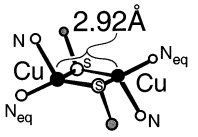

(Chart I)

Fig. 9 compares the electronic absorption and low temperature MCD spectra of the MV model to the spectra of a homovalent $Cu(II)_2$ analog [52,117]. The intense transition at 5560 cm^{-1}, which is present only in the MV model and not the homovalent analog, can be assigned as the $\psi \rightarrow \psi^*$ transition and quantitates the

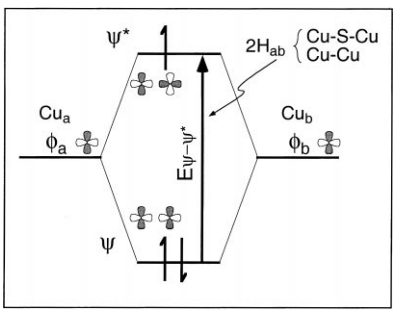

Fig. 8. Splitting of metal d orbitals in a binuclear metal complex due to a combination of superexchange through bridging ligands and direct orbital overlap and the associated ψ–ψ^* transition.

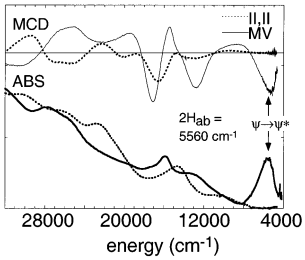

Fig. 9. Assignment of $\psi-\psi^*$ transition in the MV model complex. Comparison of low-temperature MCD (top) and absorption (bottom) spectra for the mixed valence model complex (solid lines) and the homovalent model complex (dashed lines) reveals the $\psi-\psi^*$ band at 5560 cm^{-1} that is present only in the MV complex.

electronic coupling in Fig. 8. Because of the long Cu–Cu distance, the measured value of $2H_{AB}$ (5560 cm^{-1}) for the MV model can be associated only with the superexchange pathways of the bridging thiolates. For the Cu_A site, resonance Raman excitation profiles of the accordion bending mode at ca. 130 cm^{-1} [118,119] that involves motion of the Cu nuclei of the Cu_2S_2 core, facilitate the assignment of the intense low energy (13 400 cm^{-1}) band in the Cu_A absorption spectrum (Fig. 10(A)) as the $\psi \rightarrow \psi^*$ transition [52]. The $\psi \rightarrow \psi^*$ transition, which defines $2H_{AB}$ [109,110], has shifted up in energy in the Cu_A site, relative to the MV model by 7800 cm^{-1}. Parallel sulfur K-edge studies revealed similar pre-edge absorption intensities for both Cu_A and MV model, Fig. 10(B) [120–124]. This intensity probes the amount of sulfur character in the ψ^* (HOMO) orbital and thus is a direct probe

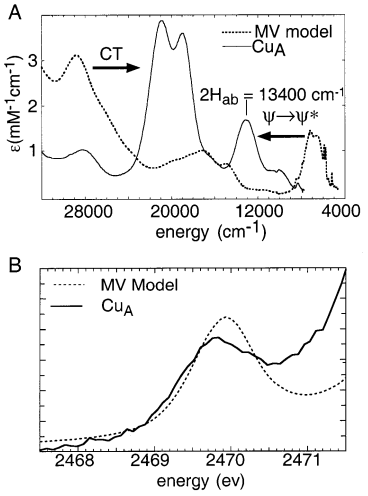

Fig. 10. Spectroscopic definition of the electronic structure of Cu_A. (A) Comparison of absorption spectra shows an increase in $\psi-\psi^*$ transition energy relative to the mixed valence model. (B) Sulfur K-edge XAS reveals similar bridging thiolate covalency in Cu_A center and the MV model.

of the superexchange contribution to bonding, which is very similar for both mixed valence centers. Thus, the difference between $2H_{AB}$ for Cu_A (Cu–Cu distance of ca. 2.4 Å [10,11]) and the MV model (Cu–Cu distance of ca. 2.9 Å [116]) must be due to an additional direct Cu–Cu bonding contribution in Cu_A that contributes ca. 7800 cm^{-1} to the electronic coupling interaction between the copper ions.

Valence delocalization in mixed valence dimers like Cu_A is opposed by vibrational distortions in the antisymmetric combination of breathing distortions of ligation spheres of the two copper ions [27,125] (the Q_- mode in the PKS description [126], where the magnitude of the distortion is given by the dimensionless coordinate x_- [126]). This out-of-phase breathing distortion lowers the energy to trap the extra electron on either Cu center. From a normal coordinate analysis of resonance Raman vibrational data [52], combined with EXAFS-derived changes in Cu–ligand bond lengths upon reduction of Cu_A [11,127], the vibronic coupling term, Λ^2/k_- [126], can be estimated for both the Cu_A center (2450 cm^{-1}) and the MV model (2190 cm^{-1}). Combining this term with the experimentally-determined electronic coupling matrix element (H_{AB}, vide supra) gives the total potential energy surfaces for the mixed valence systems [27,125]:

$$E_{\pm}(x_-) = \frac{1}{2}\left(\frac{\Lambda^2}{k_-}\right)x_-^2 \pm \left[\frac{1}{2}\left(\frac{\Lambda^2}{k_-}\right)^2 x_-^2 + H_{AB}^2\right] \quad (3)$$

Footnote [126] defines the terms in this equation [27,125]. As shown in Fig. 11, both Cu_A and the MV model have a single symmetric minimum indicating complete electron delocalization. However, it is important to note that for the Cu_A center the additional contribution to H_{AB} due to Cu–Cu bonding greatly stabilizes the delocalized state. This makes a major contribution toward keeping the Cu_A center delocalized even in the low symmetry protein environment. This delocalization should significantly increase the reduction potential of the binuclear Cu site compared to a dithiolate monomeric Cu center due to the increased positive charge delocalized over the dimer, e.g. $[Cu(SR)_2]^0$ versus $[Cu_2(SR)_2]^+$. This would be important in tuning the potential into the functionally relevant ca. 250 mV region even with the two thiolate ligands which stabilize the oxidized site [52].

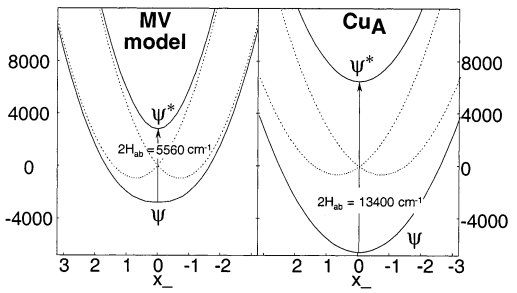

Fig. 11. Potential energy surfaces for Cu_A and the MV model showing the strong stabilization for valence delocalization in Cu_A due to metal–metal bonding.

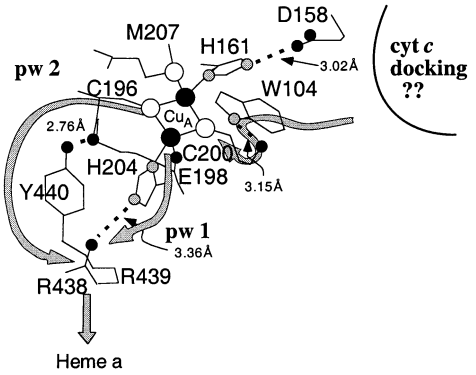

Fig. 12. Possible intra- and interprotein ET pathways involving the Cu_A center in COX. Cys thiolate covalency quadratically enhances H_{AB} for pathways (pw) involving this ligand. This makes rates involving pw1 and pw2 (indicated in figure) from Cu_A to heme *a* competitive and could provide an efficient input ET pathway from cytochrome *c* to Cu_A.

Based on our studies on the blue copper site [50], the high covalency of the thiolate bridges of the Cu_A center can provide two superexchange pathways for ET, one to the heme *a* acceptor site [52], which could be approximately competitive with a shorter His pathway [105,128] as only approximately 1% N-His [129] is contained in the HOMO, and a second from the cytochrome *c* donor site (Fig. 12) [52]. The latter is important to consider for Cu_A as this center is more buried (ca. 9 Å) from the protein surface relative to plastocyanin (ca. 4.5 Å). Further, a surface exposed Trp residue (W104 of subunit II, beef heart numbering), which has been shown to be critical for cytochrome $c \rightarrow Cu_A$ ET (and not docking) [130], is hydrogen bonded to one of the bridging Cys residues. Thus, the presence of a Cu–Cu bond in Cu_A, which maintains a delocalized ground state in the protein, should be functionally significant.

With the presence and importance of a Cu–Cu bond in Cu_A established [52], we focus on structural features of the ligand field at the Cu site which play an important role in its formation. Fig. 13A, A′ correlates the low temperature MCD spectra of the Cu_A center and the MV model [52]. The MCD spectra allow the assignments of many of the ligand field dimer states of the binuclear sites, where the symmetric and antisymmetric combinations of d orbitals on the two copper ions are split in energy due to superexchange and direct M–M overlap. These dimer splittings can be estimated from the spectra and other data from which the ligand field splittings of the d orbitals on each Cu center can be extracted [52]. From the energy levels of hypothetical monomeric fragments (Fig. 13C, C′), the xy/x^2-y^2 splitting is greatly reduced and the z^2 orbital is significantly lowered in energy in Cu_A relative to the MV model. This reflects a more trigonal ligand field at the Cu_A center where the axial ligand interaction is greatly reduced. The axial ligands in the MV model are nitrogen at a bond length of 2.13 Å [116], and for Cu_A a S(Met) at ca. 2.5 Å and a carbonyl O which appears to show some variation in Cu–O distance and is reported to be in the range 2.2–2.8 Å [12–16,131]. Importantly, the

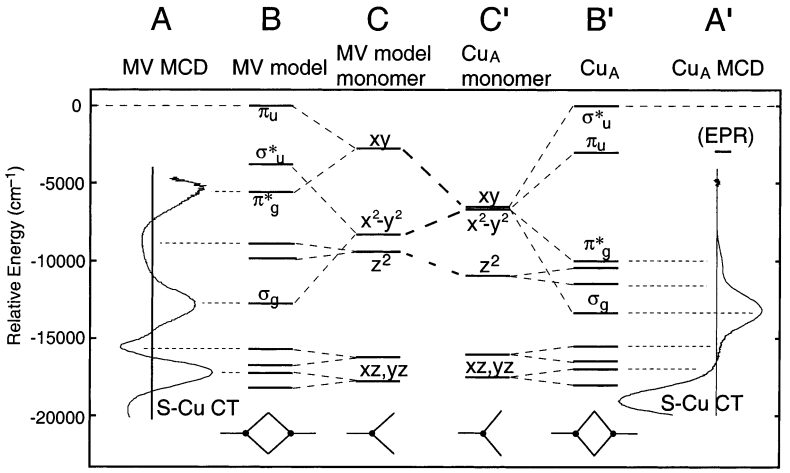

Fig. 13. Ligand field effects in Cu_A relative to the MV model. (A, A′) Low temperature, ligand field region MCD spectra of the MV model and Cu_A. (B, B′) Dimeric energy level diagrams for the MV model and Cu_A. (C, C′) Ligand field splitting pattern for hypothetical monomeric fragments of the MV model and Cu_A sites.

reduction in the splitting of the xy and x^2-y^2 hypothetical parent orbitals in Cu_A allows the significant metal–metal ψ–ψ^* interaction to overcome the ligand field splitting of the d orbitals and this changes the nature of the ground state. This is observed in the HOMOs represented by the contours in Fig. 14 (and the differences in the thiolate→Cu CT transitions in Fig. 10) [52]. The xy derived ψ^* HOMO ground state of the MV model only has superexchange pathways through the bridging thiolate ligands while the x^2-y^2 derived ψ^* ground state of Cu_A has direct metal orbital overlap forming a relatively weak σ bond [132,133]. This change in ground state is thus a direct consequence of differences in ligand field at the binuclear Cu sites.

As with blue copper, the long axial ligand–Cu bond length in Cu_A decreases its donor interaction with the Cu which is compensated by the equatorial ligands, in particular by contraction of the His–Cu bond [52]. This increases the ligand field at

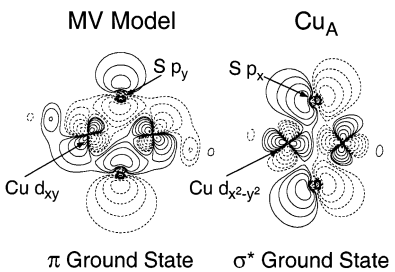

Fig. 14. The redox-active, half-filled HOMOs of the MV model (left) and Cu_A (right) calculated with Xα-SW.

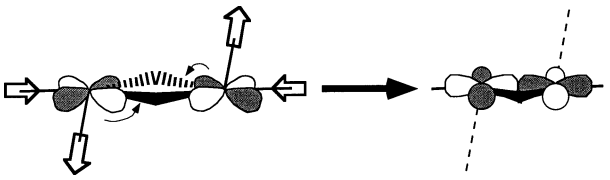

Fig. 15. Effects of the ligand field on the Cu_A center relative to the MV model. Equatorial HisN charge compensates for a weakened axial interaction resulting in HOMO rotation and formation of a Cu–Cu bond.

the copper and rotates the $x^2 - y^2$ orbital, which leads to direct σ overlap, the formation of a metal–metal bond, and produces an additional contribution to electron delocalization (Fig. 15). This description of protein ligand field control over copper–copper bonding in the Cu_A center [52] is also supported by Xα-SW DFT calculations [52] where the effects upon the HOMO were correlated with the individual geometric changes observed between the MV model and the Cu_A site. Thus, as in the entatic/rack-induced state concept in blue copper [59,60], the protein can directly affect the electronic structure of the $Cu_2(SR)_2$ center, in particular, by effecting the formation of a Cu–Cu bond through influencing the ligand interactions with the copper centers.

4. Delocalization in biologically relevant Fe(II)Fe(III) dimers

The binuclear Fe–S ET centers present in nature are the ferredoxins, which utilize the Fe(III)Fe(III)/Fe(III)Fe(II) redox couple. In the reduced state these centers are class II mixed valence with an $S_T = 1/2$ ground state derived from antiferromagnetic coupling of a high-spin Fe(III) ($S_i = 5/2$) and a high-spin Fe(II) ($S_i = 2$) (vide infra) [22,27,35], Alternatively, there is a model complex (Chart II) prepared by Wieghardt, Chaudhuri and co-workers [134], which is completely delocalized class III mixed valence and has an $S_T = 9/2$ ferromagnetic ground state [135–137]. Here we consider how the magnetic coupling relates to the delocalization and the factors, which differ between these complexes leading to their large change in ground state properties.

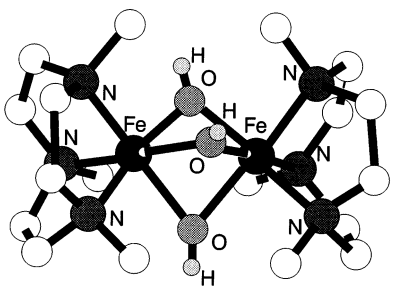

(Chart II)

In binuclear, mixed valence compounds having only one unpaired electron such as Cu_A where in each resonance structure ($[M^nM^{n+1} \leftrightarrow M^{n+1}M^n]$) one metal center is diamagnetic, there can be two interactions between the metal centers: electronic coupling (H_{AB}, also called resonance splitting) and vibronic coupling [138]. This is the case for the mixed valence Cu(I)Cu(II) dimers in the previous section and, for example the classical Creutz–Taube ion which is mixed valence and contains a low-spin Ru(II) and a low-spin Ru(III) in each resonance structure [139–141]. For mixed valence compounds in which both metal centers are paramagnetic an additional interaction has to be considered, namely electron exchange [27].

Electron exchange in homovalent compounds leads to the well-known Heisenberg–Dirac–van Vleck (HDvV) spin coupling term ($H = -2J(S_1S_2)$) in the spin Hamiltonian formalism [35,142–146]. This is observed in the oxidized state of ferredoxins $[2Fe–2S]^{2+}$ where two high spin Fe(III) ions ($S_i = 5/2$) are antiferromagnetically coupled resulting in a total spin of $S_T = 0$ for the dimer ground state. This coupling is mediated by a superexchange mechanism [112] through the bridging sulfides.

The addition of electronic coupling, H_{AB}, to electron exchange in paramagnetic mixed valence compounds leads to further splitting of the HDvV spin states with the extra electron on either half of the dimer into symmetric and antisymmetric delocalized wavefunctions. This resonance-delocalization process entails electron transfer between the iron ions and is spin dependent stabilizing the states with larger values of S_T. This additional interaction is called double exchange (or spin dependent delocalization) [27,147–155]. The underlying physical picture is given in Fig. 16, which shows that the delocalization yields maximal spin polarization stabilization energy when the unpaired electrons on each ion are aligned in a net ferromagnetic configuration [26]. In the spin Hamiltonian formalism, double exchange is included as an additional term depending on S_T, which leads to the following energies where B is the double exchange parameter [27]:

$$E_{\pm}(S_T) = -JS_T(S_T+1) \pm B(S_T+1/2) \quad (4)$$

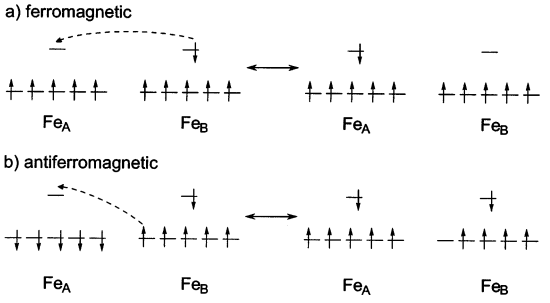

Fig. 16. Delocalization of the extra electron in the reduced, mixed valence form of an Fe(III)Fe(II) dimer. There is loss of spin polarization energy for the antiferromagnetic ground state (b) but not for the ferromagnetic ground state (a).

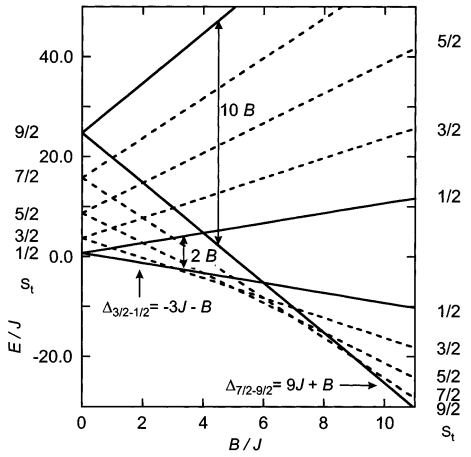

Fig. 17. Energies of the spin states for an Fe(III)Fe(II) dimer as a function of the ratio of HDvV coupling, J, to double exchange, B. Relevant energy splittings mentioned in the text are indicated.

The effect of the interplay between the HDvV coupling and double exchange is illustrated in Fig. 17 where the energies of the spin states are plotted versus the ratio of B/J (for $J<0$, i.e. antiferromagnetic coupling). For $B/J=0$ the usual spin ladder for an antiferromagnetically coupled Fe(II)Fe(III) dimer is obtained. With increasing B/J every spin state splits into two components where the splittings ($2B(S_T+1/2)$) are larger for larger total spin S_T. Thus, the ferromagnetic $S_T=9/2$ state becomes ground state for $B/J>9$.

As described in Section 3, vibronic coupling can lead to double well potential energy surfaces which corresponds to localization of the excess electron (i.e. class II mixed valence behavior). This effect is more pronounced in the lower spin states than in the higher spin states since double exchange splitting goes as $\pm B(S_T+1/2)$ which increases with S_T and opposes vibronic coupling. Therefore, strong antiferromagnetic HDvV coupling which lead to ground states with lower spin favors localization. Quantitatively, inclusion of vibronic coupling into the spin Hamiltonian formalism (Eq. (4)) yields the following energies (Λ, k_-, and x_- are defined in Section 3 [126]) [27]:

$$E_{\pm}(S_T) = -JS_T(S_T+1)+\frac{1}{2}\left(\frac{\Lambda^2}{k_-}\right)x_-^2 \pm \sqrt{\frac{1}{2}\left(\frac{\Lambda^2}{k_-}\right)^2 x_-^2 + B^2\left(S_T+\frac{1}{2}\right)^2} \qquad (5)$$

Fig. 18 gives the effects of vibronic coupling on the dimer spin states (lower energy roots of Eq. (5)) of an antiferromagnetically coupled Fe(III)Fe(II) complex. The ground state is $S_T=1/2$ which has a double well and thus is localized or trapped valent (class II) while the excited spin states are less trapped, and in the $S_T=9/2$ case there is one minimum at the symmetric geometry ($x_-=0$) indicating complete delocalization (class III).

We can now consider the [2Fe–2S] ET center in ferredoxin which has a localized Fe(III)Fe(II) $S_T=1/2$ ground state [22] and evaluate factors in Eq. (5), which differ

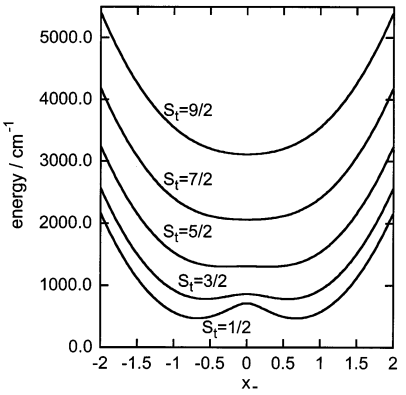

Fig. 18. Ground and excited spin-state potential energy surfaces in the antisymmetric reduced normal coordinate x_- for an Fe(III)Fe(II) dimer. Calculated using Eq. (5) with $J = -150\ cm^{-1}$, $B = 300\ cm^{-1}$, $\Lambda^2/k_- = 2000\ cm^{-1}$. As the total spin increases from $S_T = 1/2$ to 9/2, valence delocalization becomes increasingly favored as indicated by the single minimum in the potential energy surface of the $S_T = 9/2$ state.

relative to the tris-μ-hydroxo bridged, 1,4,7-trimethyl-1,4,7-triazacyclononane (L) capped iron dimer, $[LFe(\mu_2\text{-}OH)_3FeL]^{2+}$ (Chart II), which exhibits a valence delocalized $S_T = 9/2$ ferromagnetic ground state [134–137]. These differences in electron delocalization can be understood by investigating the metal centered excited states which provide direct experimental probes of orbital pathways for electron delocalization and superexchange [109,110].

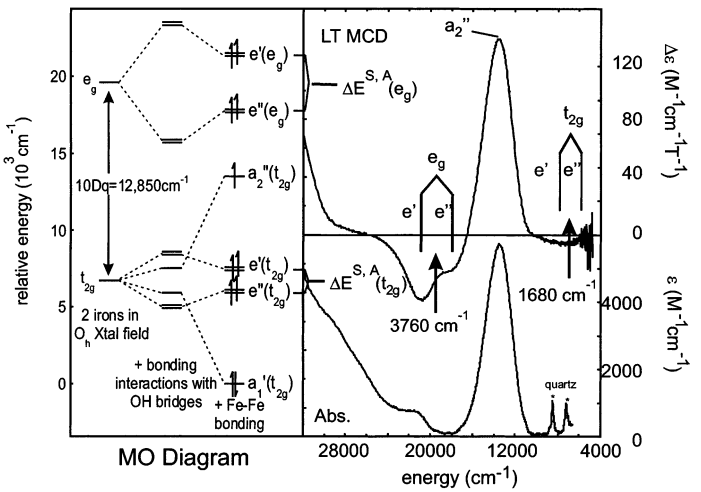

Fig. 19. Left: molecular-orbital splitting diagram for $[LFe(OH)_3FeL]^{2+}$ based on an angular-overlap approach in conjunction with the observed electronic transitions. Right: low-temperature MCD spectrum (top) and absorption spectrum (bottom) of $[LFe(OH)_3FeL]^{2+}$ in 50:50 propionitrile–butyronitrile glass. Band assignments refer to the MO diagram in the left panel [109].

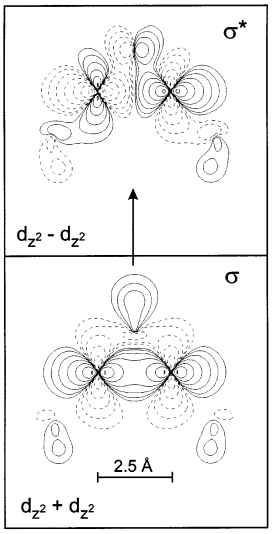

Fig. 20. Contour plots of the molecular orbitals associated with the z^2 bonding → antibonding transition from an SCF-Xa-SW calculation of $[LFe(OH)_3FeL]^{2+}$. The plots are in the Fe–(OH)–Fe plane.

Fig. 19 presents the low temperature absorption and MCD spectra of $[LFe(\mu_2\text{-}OH)_3FeL]^{2+}$ with specific band assignments indicated at the top which derive from the selection rules for absorption, MCD, and resonance Raman depolarization ratios [109,110]. These band assignments relate to the angular overlap generated energy level diagram on the left hand side of Fig. 19, which shows the splitting of the octahedral set of d orbitals (t_{2g}, e_g, far left) into symmetric and antisymmetric combinations in the dimer due to superexchange interactions with the bridging hydroxides (middle) and direct metal–metal bonding interactions (right). The resulting ten dimer molecular orbitals are occupied by 11 electrons to produce the $S_T = 9/2$ ground state with the extra electron in the bonding combination of z^2 orbitals (the z-axis is along the Fe–Fe axis). The transition to the z^2 antibonding combination (the 13 500 cm^{-1} band labeled $a_{2''}$ in the spectra of Fig. 19) is a direct probe of the electronic coupling associated with delocalization of the extra electron and is thus a measure of $2H_{AB}$ ($10B$ for the $S_T = 9/2$ state, where B is again the double exchange parameter that defines the contribution of electron delocalization in the spin-Hamiltonian formalism (Eq. (4))).

Density functional calculations calibrated with the experimental data for this transition show that $90 \pm 7\%$ of $2H_{AB}$ derives from the direct overlap of two z^2 orbitals at an Fe–Fe distance of 2.51 Å. The contour plots of the molecular orbitals associated with this bonding → antibonding transition are given in Fig. 20. An absorption bandshape analysis combined with resonance Raman spectroscopy establish a probe of the excited state distortions associated with this $\sigma \rightarrow \sigma^*$ transition [109,110]. Upon excitation into this band, both a_1' core vibrations are resonance enhanced, the in phase breathing mode at 316 cm^{-1} and the out of phase

accordion distortion at 124 cm^{-1} (Fig. 21). These vibrations were used to fit the low-temperature absorption bandshape, its temperature dependence and the resonance Raman excitation profiles (Fig. 22), allowing for excited state distortions of anharmonic potential energy surfaces. From this analysis, an accurate estimate of the excited state geometry (Fig. 23) was obtained. These studies show that there is a large increase in the Fe–Fe distance (0.4 Å, Fig. 22 bottom) consistent with the loss of a direct M–M bond. These potential energy surfaces can further be used to obtain an experimental estimate of the dependence of $2H_{AB}$ ($10B$) on Fe–Fe distance (r). From Fig. 23 an estimate of $\Delta B/\Delta r$ is 1750 cm^{-1}/Å. These studies show that the B value for $[LFe(\mu_2\text{-}OH)_3FeL]^{2+}$ ($r = 2.51$ Å) is 1,350 cm^{-1}, and on going to the $[2Fe\text{–}2S]^{+}$ dimer ($r = 2.73$ Å) B decreases to ca. 965 cm^{-1} [156], which is still a sizable contribution to electron delocalization due to direct d_{z^2} orbital overlap in the Fe–S dimer [109,110].

As indicated above, this electronic coupling is opposed by antiferromagnetic exchange coupling, which can also be estimated from excited-state spectroscopy. Fig. 17 allows for the combined effects of antiferromagnetic coupling and double exchange on the mixed valence iron dimer ground state and shows that an $S_T = 1/2$ occurs for $B/J < 3$ while an $S_T = 9/2$ is the ground state for $B/J > 9$. For an $S_T = 9/2$ ground state, the $S_T = 7/2$ first excited state is at an energy $\Delta_{7/2-9/2} = 9J + B$. From SQUID magnetic susceptibility data for $[LFe(\mu_2\text{-}OH)_3FeL]^{2+}$ in Fig. 24, there is no deviation in μ_{eff} above the error limits at high temperature indicating that $\Delta_{7/2-9/2} > 720$ cm^{-1}. With the B value of 1350 cm^{-1} (vide supra), this gives $-J < 70$ cm^{-1}. This exchange coupling is associated with super-exchange pathways between half occupied magnetic orbitals on the two irons which are also observed directly in the electronic spectrum. From Fig. 19, the symmetric-antisymmetric splitting ($\Delta E^{S,A}$) of the e(σ) orbitals is 3460 cm^{-1} and that of the e component of the $t_{2g}(\pi)$ set is 1680 cm^{-1}. Using these experimental values along with reasonable estimates of the Coulomb and exchange integrals in the Hay, Thibeault, Hoffmann model [108] which relates $(\Delta E^{S,A})^2$ to J:

$$J = K_{ab} - \frac{1}{2}\sum_i \frac{(\Delta E_i^{S,A})^2}{J_{aa} - J_{ab}} \tag{6}$$

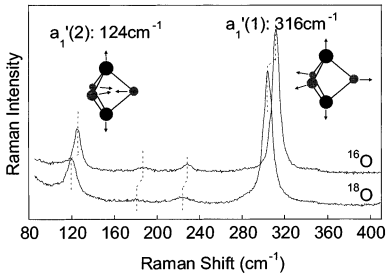

Fig. 21. Solid-state resonance Raman scattering of $[LFe(^{16}OH)_3FeL]^{2+}$ and $[LFe(^{18}OH)_3FeL]^{2+}$ at ca. 120 K using 568 nm excitation. Included are depictions of the $a_1'(1)$ and $a_1'(2)$ normal mode solutions from a normal mode analysis based on the observed isotopic shifts [109,110].

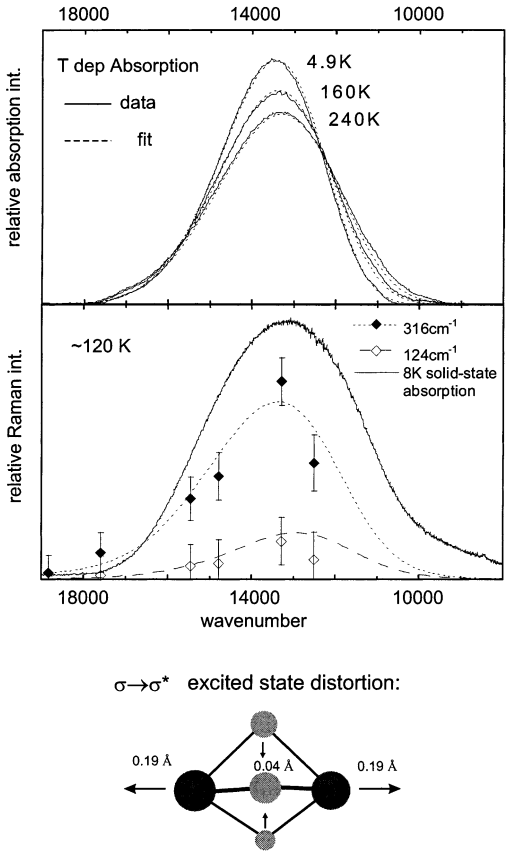

Fig. 22. Top: experimental (solid line) and simulated (dashed line) variable-temperature solution near-IR absorption spectra of $[LFe(OH)_3FeL]^{2+}$. Middle: experimental and ca. 120 K solid state resonance Raman excitation profiles of the 316 and 124 cm^{-1} vibrational modes of $[LFe(OH)_3FeL]^{2+}$. The 8 K solid-state absorption spectrum is superimposed. Simulations are calculated using Lennard-Jones potentials. Bottom: Nuclear distortion derived for the $\sigma \rightarrow \sigma^*$ excited state [110].

(with K_{ab} is the two center-two electron exchange integral, J_{aa} and J_{ab} are the one-center and two-center two-electron coulomb repulsion integrals, respectively, and i the one-electron magnetic orbital pathways) gives an experimental estimate of $-23 \leq J \leq 2$ cm^{-1}. An estimate of J for the localized mixed valence $[2Fe–2S]^{+}$ center can be obtained from the previously reported magnetic susceptibility data [24,157], which gave a $\Delta_{3/2-1/2}$ splitting of 315 cm^{-1}, and Fig. 17, which shows that $\Delta_{3/2-1/2} = -3J - B$. The above estimated B value for $[2Fe–2S]^{+}$ (965 cm^{-1}) thus gives $J = -430$ cm^{-1}, which is much larger than the J value for $[LFe(\mu_2\text{-}OH)_3FeL]^{2+}$ and leads to the experimentally observed $S_T = 1/2$ ground state. This difference in J relates to differences in superexchange pathways where the *tris*-hydroxy bridged structure has relatively poor Fe-bridging ligand overlap due to protonation and the ca. 80° Fe–O–Fe angle while the iron sulfur dimer has highly

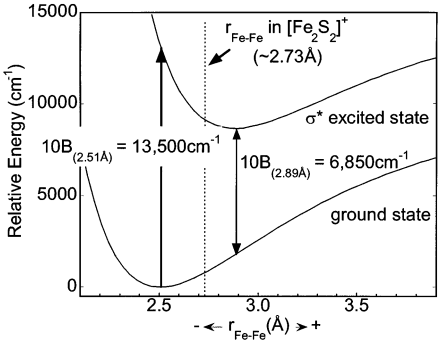

Fig. 23. Ground state and σ* excited state potential energy surfaces along the Fe–Fe vector. Effects of the nuclear distortion shown in Fig. 22 bottom on the double-exchange resonance splitting between the $S_T = 9/2$ ground and excited spin states. The dashed vertical line marks the Fe–Fe distance in $[2Fe–2S]^+$ [109].

covalent sulfide bridges (a low-valence ionization energy) which provide two efficient superexchange pathways as illustrated in Fig. 25.

Finally, these superexchange and double exchange contributions have to be combined with vibronic coupling in the Q_- mode of PKS theory. This produces a geometric distortion that can lead to valence trapping (Eq. (5)). This leads to the potential energy surfaces in Fig. 26, and the final parameter values for $[2Fe–2S]^+$ and $[LFe(\mu_2\text{-}OH)_3FeL]^{2+}$ are given in Table 1 [158]. Since the double exchange term goes as $B(S_T + 1/2)$, the $S_T = 9/2$ ground state of $[LFe(\mu_2\text{-}OH)_3FeL]^{2+}$ is delocalized while the $S_T = 1/2$ ground state of $[2Fe–2S]^+$ is localized as observed experimentally. From Table 1 the dominant contribution to localization in

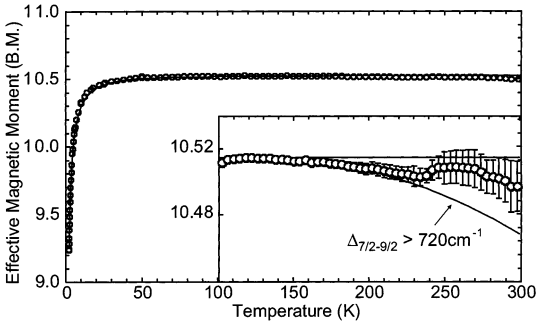

Fig. 24. Variable temperature magnetic susceptibility data of $[LFe(OH)_3FeL]^{2+}$. The solid line is the best fit of the low-temperature data using a spin system of $S = 9/2$ with $g = 2.115$ and $D = 2.28\ cm^{-1}$. Inset: High-temperature data displayed on an expanded scale. A simulated data curve (taking into account thermal occupation of the first excited spin state $S_T = 7/2$) is included showing the calculated temperature dependence for $\Delta = 720\ cm^{-1}$ [109].

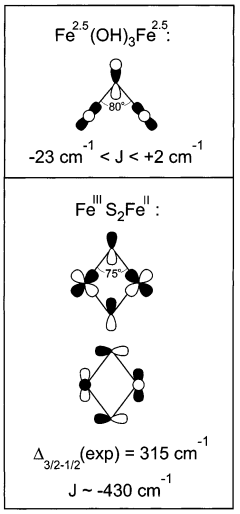

Fig. 25. Superexchange pathways for $[LFe(OH)_3FeL]^{2+}$ (top) and $[2Fe–2S]^{+}$ (bottom). The pathway for the former compound is significantly weaker than those for the latter due to reduced metal-bridging ligand covalency (hydroxo versus sulfido) and the differences in the bridging angle [109].

$[2Fe–2S]^{+}$ is the large antiferromagnetic coupling which opposes the electronic coupling associated with electron delocalization. Therefore, changes in the antiferromagnetic coupling, in particular in the higher nuclearity clusters, could affect their delocalization and hence contribute to the redox properties of these sites.

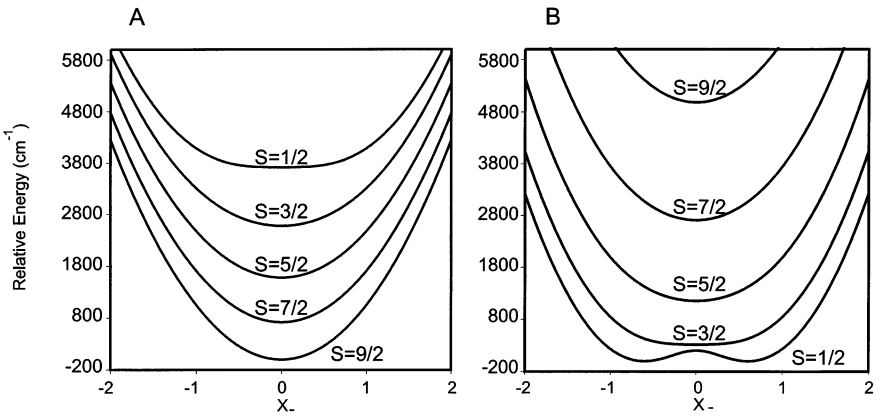

Fig. 26. Ground and excited spin-state potential energy surfaces in the $x\_$ coordinate calculated with Eq. (5) and the parameters given in Table 1, showing the valence delocalized $S_T = 9/2$ ground state for $[LFe(OH)_3FeL]^{2+}$ (A) and the valence localized $S_T = 1/2$ ground state for the $[2Fe–2S]^{+}$ dimer (B).

5. Delocalization versus localization in tetrameric versus dimeric Fe–S clusters

The [4Fe–4S] cubane cluster can be viewed as a dimer of two [2Fe–2S] clusters where one thiolate on each iron center is replaced by a sulfide, which thus becomes a μ_3-bridging ligand. Removal of one iron center from the cubane cluster gives the cuboidal [3Fe–4S] cluster with μ_3- and μ_2-bridging sulfides (Chart III).

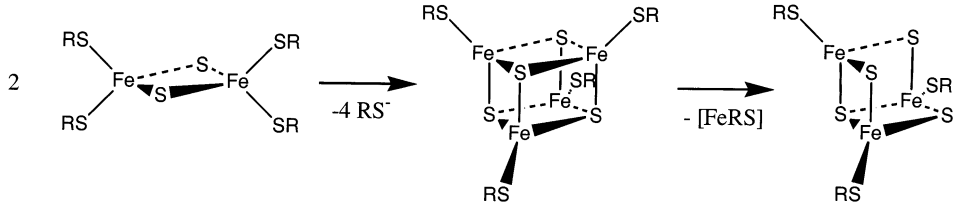

[2Fe-2S] [4Fe-4S] [3Fe-4S]
(Chart III)

In the reduced mixed valence $[3Fe–4S]^0$ form of ferredoxin II of *Desulfovibrio gigas* comprised of formally two Fe(III) and one Fe(II), the excess electron is delocalized over a pair of iron centers leading to a $Fe_2(2.5)$ subsite (class III mixed valence) with an $S = 9/2$ pair ground state which is antiferromagnetically coupled to the remaining Fe(III) ($S = 5/2$) to generate the observed $S_T = 2$ ground state of the trinuclear cluster [150,159,160]. In the cubane-type core structures, which mostly function in two of three oxidation states, $[4Fe–4S]^{3+,2+,1+}$ [161], such a class III delocalized mixed valence $Fe_2(2.5)$ pair with an $S = 9/2$ ground state occurs for all three oxidation levels [29,162–166]. For example an $S_T = 0$ ground state results from the antiferromagnetic coupling of two such $S = 9/2$ pairs in the $[4Fe–4S]^{2+}$ cluster [167].

Here we consider the differences between the mixed valence site in the $[2Fe–2S]^+$ dimer and the mixed valence sub-site of the $[4Fe–4S]^{2+}$ tetramer that lead to a valence localized pair (class II) in the dimer with an antiferromagnetic ground state (Section 4) and to a valence delocalized pair (class III) in the dimer sub-site of the tetramers with a ferromagnetic ground state. As indicated above this difference should derive from differences in superexchange and double exchange, which in turn relate to changes in covalency of the ligand–metal bond in the tetramers versus the dimers. While the high covalency of these sites makes these difficult to study by traditional spectroscopic methods, this difference can be addressed experimentally through sulfur K-edge X-ray absorption spectroscopy.

Table 1

	$[LFe(\mu_2\text{-}OH)_3FeL]^{2+}$	$[2Fe–2S]^+$
B (cm^{-1})	1350	965
J (cm^{-1})	> -70	-360
Λ^2/k_- (cm^{-1})[a]	2590	3660

[a] See Ref. [109], p. 8096 for vibronic coupling analysis.

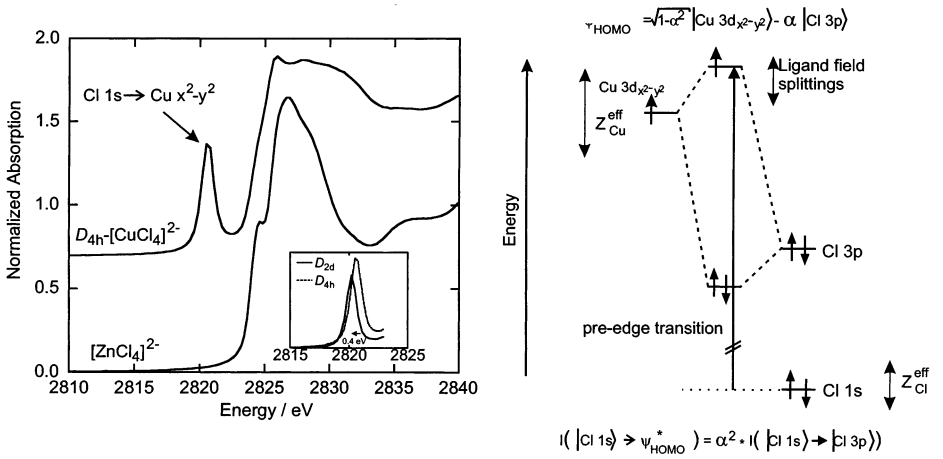

Fig. 27. Left: Cl K-edge XAS on D_{4h} $[CuCl_4]^{2-}$ and $[ZnCl_4]^{2-}$. Only in the d^9 Cu(II) compound is a pre-edge peak observable. Right: Orbital energy diagram displaying the origin of the pre-edge feature in D_{4h} $[CuCl_4]^{2-}$ as a transition from Cl 1s level into the antibonding MO comprised of mainly Cu d-character and covalently mixed Cl 3p character. The intensity is proportional to the square of the Cl 3p wave function coefficient. The inset shows a comparison of D_{4h} $[CuCl_4]^{2-}$ and D_{2d} $[CuCl_4]^{2-}$ [72].

Ligand K-edge X-ray absorption spectroscopy is a powerful new probe of ligand–metal bonding, in particular for Bioinorganic systems [72,73,168–175]. The nature of the experiment is illustrated in Fig. 27. In contrast to $[ZnCl_4]^{2-}$ (d^{10}), square planar D_{4h} $[CuCl_4]^{2-}$ (d^9) exhibits an intense pre-edge absorption peak in the Cl K-edge X-ray absorption spectrum at 2820 eV corresponding to a Cl 1s → Cu x^2-y^2 transition [72]. Due to the localized nature of the Cl 1s orbital, this transition intensity is associated with the electric dipole allowed chloride 3p character mixed into the half occupied metal x^2-y^2 HOMO due to bonding. An experimental estimate of this mixing for D_{4h} $[CuCl_4]^{2-}$ was obtained using a variety of spectroscopic methods which quantifies the intensity of the pre-edge feature in Fig. 27 as corresponding to 39% Cl 3p character in the half occupied HOMO. The energy of the pre-edge transition has three contributions: (1) the chemical shift of the Cl 1s core orbital due to ligand charge donation; (2) the ligand field splitting of the d orbitals; and (3) the largest which is the shift of the d manifold due to changes in Z_{eff} of the metal ion. The insert in Fig. 27 illustrates the effect of changing the geometry to a D_{2d} distorted tetrahedral structure on the pre-edge feature. The energy goes down due to the decreased ligand field splitting in the D_{2d} structure, and the intensity decreases indicating a decrease of the covalency of the x^2-y^2 orbital. Based on the quantitative intensity change between D_{4h}- and D_{2d}-$[CuCl_4]^{2-}$, the ground state of the distorted tetrahedral structure has 30% Cl 3p character.

In order to apply ligand K-edge X-ray absorption spectroscopy to metal complexes with more than one hole in the d-manifold, this method was extended to a series of metal tetrachlorides [169]. To quantify the covalency from the intensity of the pre-edge feature of the d^n $[MCl_4]^{2-}$ complexes, one needs to consider transi-

tions from the Cl 1s to both the partially occupied t_2 and e covalently mixed molecular orbitals which has been done using the irreducible tensor method. This intensity is distributed over a series of d^{n+1} final states using multiplet effects in ligand field theory. The experimentally determined pre-edge intensity gives a total covalency distributed over the five half occupied d orbitals of 85.5% for $[Fe(III)Cl_4]^-$ which results in 21% per Fe(III)–Cl bond.

The study was then extended to the sulfur K-edge (ca. 2470 eV) of a series of d^n tetrathiolates [170]. Using the pre-edge of blue copper as a reference (38% thiolate S 3p character, see Fig. 3(A)) [73] and renormalizing for four coordinated sulfurs, the intensity of the pre-edge gives a total thiolate covalency over the half occupied d orbitals of 151% in $[Fe(III)(SR)_4]^-$ (Fig. 28, solid line), or 38% per RS–Fe(III) bond. This experimentally quantifies the fact that the thiolate ligand is more covalent than the chloride (38 versus 21%) even though it has one less π valence orbital for bonding. It is also of interest to compare the pre-edge feature of the tetrathiolate model to those of three rubredoxins (Fig. 28) [171]. In all cases, the intensity of the protein site is lower indicating reduced covalency (129% versus 151% total). This correlates with the fact the rubredoxins each have six H-bonds to the thiolate ligands which reduces their donor strengths. This destabilizes the oxidized site and should (along with the protein dielectric, dipoles etc. [37]) contribute to the generally higher reduction potentials of the protein sites relative to model complexes.

In order to extend these studies to the Fe–S clusters, the differences between the two kinds of sulfur ligand present in the clusters needed to be considered: terminal thiolates and bridging sulfides. Due to different effective nuclear charges of these two types of sulfur atoms the pre-edge transitions are nicely resolved in dimeric model compounds (Fig. 29(a)) with the sulfide pre-edge feature at lower energy due to the lower effective nuclear charge of sulfide compared to thiolate [172]. To quantify sulfide pre-edge intensity, $CsFeS_2$ and $KFeS_2$, which are linear chains of

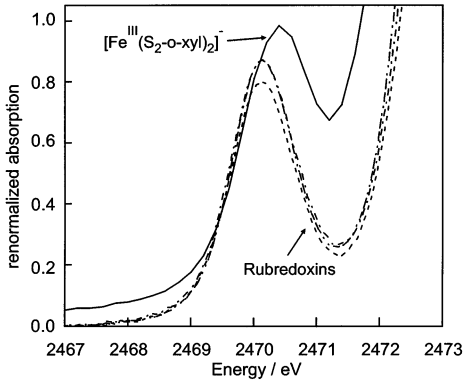

Fig. 28. S K-edge XAS spectra of a ferric tetrathiolate model compound and three different rubredoxins. The pre-edge intensity of the rubredoxins is reduced compared to the model compound indicating H-bonding in the protein matrix [171].

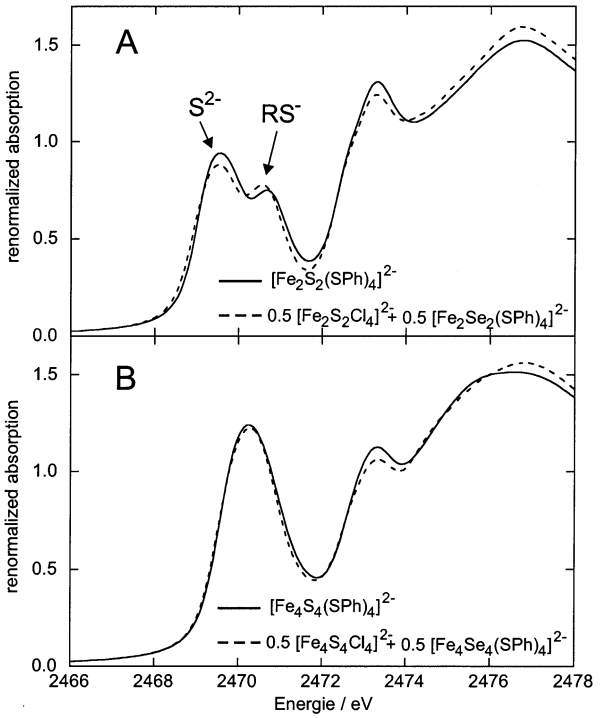

Fig. 29. S K-edge XAS spectra of $[Fe_nS_n(SPh)_4]^{2-}$ (solid lines; A: $n=2$; B: $n=4$) and renormalized addition spectra (dashed line) of the exclusively thiolate sulfur containing $[Fe_nSe_n(SPh)_4]^{2-}$ and the exclusively sulfide sulfur containing $[Fe_nS_nCl_4]^{2-}$ [171].

ferric sites bridged by two μ_2-sulfides were used as a reference [176]. The intensity of the pre-edge of $CsFeS_2$ quantifies the ferric sulfide as having 225% total covalency, which gives 56% per sulfide–Fe(III) bond. This experimentally demonstrates that the sulfide is more covalent than the thiolate, and from the shape of its pre-edge feature, this in part reflects an additional π donor interaction for the sulfide.

Using the thiolate and sulfide complexes described above as references, the S K-edge X-ray absorption spectra of the binuclear ferric model complexes $[Fe_2S_2(SR)_4]^{2-}$ (Fig. 29(a)) yield experimental values for the covalency of the iron-sulfur bonds. From the intensities of the pre-edge features in $[Fe(III)_2S_2(SR)_4]^{2-}$, each RS^-–Fe(III) bond has 24% covalency relative to 38% for $[Fe(III)(SR)_4]^-$, and each S^{2-}–Fe(III) bond has 72% covalency (relative to 56% for $CsFeS_2$). Thus replacing two thiolates with sulfides decreases the covalency of the remaining thiolate-Fe(III) bonds, and replacing two bridging sulfides with thiolates increases the remaining sulfide donor interactions, again demonstrating the greater covalent donor interaction of sulfide relative to thiolate. Terminal ligands can therefore be used as spectator ligands reflecting the electron donation from the remaining ligand set (vide infra).

These S K-edge studies have now been extended to the [4Fe–4S] clusters [174]. Going from [2Fe–2S] to [4Fe–4S] involves replacing one thiolate on each Fe with the bridging sulfides of a second dimer, resulting in the formation of μ_3-sulfide bridges in the tetramers as compared to μ_2-sulfide bridges in the dimers (Chart III). We have been interested in defining the changes in bonding which occur between the dimer and tetramer that could affect delocalization and the redox properties of these clusters. The measured S K-edge X-ray absorption spectra for $[Fe_4S_4(SR)_4]^{2-}$, $[Fe_4S_4Cl_4]^{2-}$, and $[Fe_4Se_4(SR)_4]^{2-}$ and the renormalized sum of the S K-edges of the selenide and chloride, which reproduces that of $[Fe_4S_4(SR)_4]^{2-}$, are shown in Fig. 29(B) (R = Ph). In comparison to the dimer spectra in Fig. 29(A), the sulfide peak has shifted to higher energy so that the pre-edge transitions of the thiolate and the sulfide are no longer clearly resolved.

This comparison of the pre-edge features of $[Fe_4(2.5)S_4(SPh)_4]^{2-}$ to those of $[Fe(III)_2S_2(SR)_4]^{2-}$ is complicated by two major differences which affect the energies and intensities of the pre-edges: 1) the formal oxidation states change from $+2.5$ to $+3$ and 2) the bridging sulfide change from a μ_2- to a μ_3-mode. In order to independently evaluate the changes associated only with the bridging mode and to define differences in electronic structure that could contribute to delocalization in the tetramer, we compare the pre-edge of $[Fe_4(2.5)S_4(SPh)_4]^{2-}$ to that of a hypothetical delocalized mixed valence μ_2-sulfide dimer $[Fe_2(2.5)S_2(SPh)_4]^{2-}$. Fig. 30(A) gives the results for the chloride edges in $[Fe_4(2.5)S_4Cl_4]^{2-}$ and the hypothetical $[Fe_2(2.5)S_2Cl_4]^{3-}$ dimer which was estimated as follows: Comparison of the pre-edge of $[Fe(III)Cl_4]^{-}$ with that of $[Fe(III)_2S_2Cl_4]^{2-}$ gives the effects of replacing two chlorides with two μ_2-sulfides. This can be used in combination with trends from density functional calculations to estimate the Cl pre-edge feature of $[Fe(II)_2S_2Cl_4]^{4-}$ from that of $[Fe(II)Cl_4]^{2-}$, which is observed experimentally. The average of the energies and intensities of the $[Fe(III)_2S_2Cl_4]^{2-}$ and $[Fe(II)_2S_2Cl_4]^{4-}$ pre-edge features then gives the predicted spectrum of the hypothetical $[Fe_2(2.5)S_2Cl_4]^{3-}$ delocalized μ_2-sulfide bridged dimer (class III) [174]. Comparison to the Cl K-edge spectrum of $[Fe_4(2.5)S_4Cl_4]^{2-}$ shows that the pre-edge of the tetramer is lower in energy and considerably more intense. This shows (1) that the Z_{eff} of the iron in the tetranuclear cluster is higher and (2) the Cl–Fe(2.5) bond is more covalent. Thus using the terminal chloride ligands as spectator ligands, the μ_3-sulfides in the tetranuclear cluster are poorer donors than the μ_2-sulfides in the dimer.

The equivalent comparison for terminal thiolate ligation has been developed using the analogous approach to estimate the pre-edge feature of $[Fe(II)_2S_2(SPh)_4]^{4-}$ and from that of $[Fe_2(2.5)S_2(SPh)_4]^{3-}$ [174]. From Fig. 30(B) the same trends as in the chloride pre-edges are observed in the pre-edges of $[Fe_4(2.5)S_2(SPh)_4]^{2-}$ and $[Fe_2(2.5)S_2(SPh)_4]^{3-}$: (1) the Z_{eff} of the iron in the tetranuclear cluster is higher and (2) the RS^{-}–Fe(2.5) bond is more covalent. Thus again, the μ_3-sulfides in the tetranuclear cluster are poorer donors than the μ_2-sulfides in the dimer.

The differences between the electronic structures of the mixed valence dimer and tetramer due to the change of sulfide bridging mode can also be seen directly in a

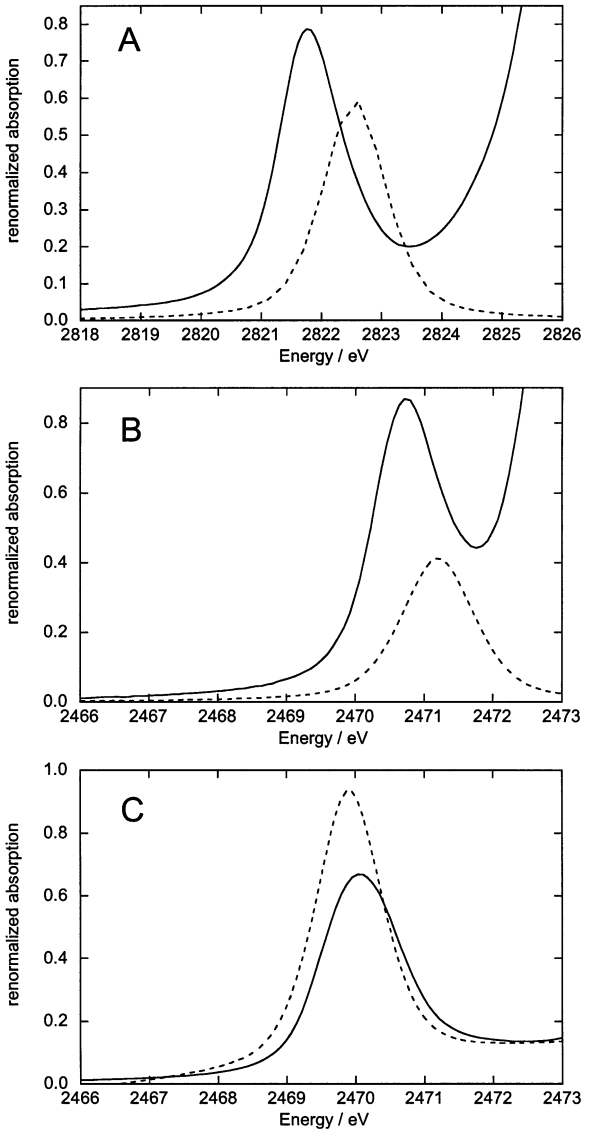

Fig. 30. A: Cl K-edge XAS spectra of $[Fe_4(2.5)S_4Cl_4]^{2-}$ (solid line) and the hypothetical, valence delocalized $[Fe_2S_2Cl_4]^{3-}$ (dashed line); B: S K-edge XAS spectra of $[Fe_4(2.5)Se_4(SPh)_4]^{2-}$ (solid line) and the hypothetical, valence delocalized $[Fe_2(2.5)Se_2(SPh)_4]^{3-}$ (dashed line); C: S K-edge XAS spectra of $[Fe_4S_4C_4]^{2-}$ (solid line) and the hypothetical, valence delocalized $[Fe_2(2.5)S_2Cl_4]^{3-}$ (dashed line). The spectra show the dependence on the chloride- (A), thiolate- (B), and sulfide- (C) ligands due to changing the bridging sulfides from a μ_2- to a μ_3-bridging mode. The construction of the spectra for the hypothetical dimers is explained in the text [174].

comparison of the sulfide pre-edge features in $[Fe_4(2.5)S_2Cl_4]^{2-}$ and $[Fe_2(2.5)S_2Cl_4]^{3-}$ [174]. The hypothetical $[Fe_2(2.5)S_2Cl_4]^{3-}$ spectrum (Fig. 30(C)) is estimated from the energies and intensities from the spectra of $[Fe(III)_2S_2Cl_4]^{2-}$, $CsFe(III)S_2$, $Ba_2Fe(II)S_3$, and $[Fe(II)_2S_2Cl_4]^{4-}$ and trends from density functional calculations. In contrast to the chloride (Fig. 30(A)) and thiolate (Fig. 30(B)) pre-edges, the sulfide pre-edge peak of the hypothetical dimer $[Fe_2(2.5)S_2Cl_4]^{3-}$ is more intense than the pre-edge peak of the tetramer $[Fe_4(2.5)S_2Cl_4]^{2-}$ and at lower energy (Fig. 30(C); note that all intensities are renormalized to reflect the intensity per $Fe–S^{2-}$ bond). The reduced intensity in the spectrum directly reflects the reduced covalency of the Fe-μ_3-S^{2-} bond compared to the Fe-μ_2-S^{2-} bond. The higher energy of sulfide pre-edge in the tetramer which is also in the opposite direction of the chloride and thiolate reflects a shift of the sulfide 1s binding energy. The sulfide 1s binding energy increases because the sulfide goes from μ_2- to μ_3-bridging which results in a higher total charge donation to three rather than two iron centers.

The reduced covalency should decrease the superexchange interaction of the bridging ligands with the iron center and therefore reduce the exchange coupling. The differences in the effective nuclear charge and the orientation of the orbital containing the extra electron in the tetramer versus the dimer should also affect the magnitude of the double exchange contribution [177]. Depending on their magnitudes, the combined effects of reduction of the superexchange pathway and increase of the double exchange pathway in the mixed valence tetramer could yield a class III delocalized subsite in the tetramers with an ferromagnetic $S = 9/2$ ground state. A quantitative evaluation of these effects and inclusion of vibronic coupling is now in progress.

6. Concluding comments

From the above summaries, the unique spectral features of metalloprotein redox centers are becoming well understood and reflect highly covalent active sites. The high covalency can play an important role in coupling the electron transfer center into protein pathways for long range ET (H_{DA} in Eq. (1)) and in tuning the interactions between metal centers in binuclear sites which can affect their reduction potential, E^0, and reorganization energy, λ. For these highly covalent systems, ligand K-edge X-ray absorption spectroscopy has had a large impact on our understanding of the electronic structures of all the metalloprotein ET sites considered in this review. The protein environment plays an important role in determining the geometric and, hence, electronic structures of these active sites. In iron sulfur centers, the role of the protein environment is still being developed, while in blue copper centers, it is clear that the protein contributes to the geometry of the active site as well as the position along the coupled distortion coordinate defined in Fig. 7. In the Cu_A center, the protein can influence the formation of a metal–metal bond which maintains electron delocalization in the low symmetry environment of the protein and this affects the reduction potential of the site.

Acknowledgements

This work was supported by NSF Grant CHE-952850 (E.I.S.). Grateful acknowledgement is made for postdoctoral fellowships from the NIH (to D.W.R., GM-18812) and from the Deutsche Forschungsgemeinshaft (to T.G.). We acknowledge invaluable interactions with our collaborators on various parts on research presented here: Professor K.O. Hodgson and Dr B. Hedman, Professor S. DeVries, Professor W.B. Tolman, Professor K. Wieghardt, S. DeBeer, Dr E. Bominaar, Dr D. Gamelin, Dr L. LaCroix, Dr K. Rose, and Dr S.E. Shadle.

References

[1] J.M. Nocek, J.S. Zhou, S. DeForest, S. Priyadarshy, D.N. Beratan, J.N. Onuchic, B.M. Hoffman, Chem. Rev. 96 (1996) 2459.
[2] H.B. Gray, J.R. Winkler, Annu. Rev. Biochem. 65 (1996) 537.
[3] E.T. Adman, in: C.B. Anfinsen, F.M. Richards, J.T. Edsall, D.S. Eisenberg (Eds.), Advances in Protein Chemistry, vol. 42, Academic Press, San Diego, CA, 1991, pp. 145–197.
[4] A. Messerschmidt, Structure and Bonding, vol. 90, Springer, Berlin, 1998, pp. 37–68.
[5] E.N. Baker, in: R.B. King (Ed.), Encyclopedia of Inorganic Chemistry, Wiley, Chichester, 1994, pp. 883–905.
[6] H. Beinert, Eur. J. Biochem. 245 (1997) 521.
[7] P.M.H. Kroneck, W.E. Antholine, J. Riester, W.G. Zumft, FEBS Lett. 242 (1988) 70.
[8] P.M.H. Kroneck, W.A. Antholine, J. Riester, W.G. Zumft, FEBS Lett. 248 (1989) 212.
[9] M.B. Robin, P. Day, Adv. Inorg. Chem. Radiochem. 10 (1967) 247.
[10] N.J. Blackburn, M.E. Barr, W.H. Woodruff, J. van der Oost, S. de Vries, Biochemistry 33 (1994) 10401.
[11] N.J. Blackburn, S. de Vries, M.E. Barr, R.P. Houser, W.B. Tolman, D. Sanders, J.A. Fee, J. Am. Chem. Soc. 119 (1997) 6135.
[12] T. Tsukihara, H. Aoyama, E. Yamashita, T. Tomizaki, H. Yamaguchi, K. Shinzawa-Itoh, R. Nakashima, R. Yaono, S. Yoshikawa, Science 269 (1995) 1069.
[13] T. Tsukihara, H. Aoyama, E. Yamashita, T. Tomizaki, H. Yamaguchi, K. Shinzawaitoh, R. Nakashima, R. Yaono, S. Yoshikawa, Science 272 (1996) 1136.
[14] S. Iwata, C. Ostermeier, B. Ludwig, H. Michel, Nature 376 (1995) 660.
[15] C. Ostermeier, A. Harrenga, U. Ermler, H. Michel, Proc. Natl. Acad. Sci. USA 94 (1997) 10547.
[16] P.A. Williams, N.J. Blackburn, D. Sanders, H. Bellamy, E.A. Stura, J.A. Fee, D.E. McRee, Nat. Struct. Biol. 6 (1999) 509.
[17] W. Lovenberg (Ed.), Iron–Sulfur Proteins, vol. I–III, Academic Press, New York, 1973–1977.
[18] T.G. Spiro (Ed.), Iron-Sulfur Proteins, Metal Ions in Biology, Wiley, New York, 1982.
[19] R. Cammack, T.G. Spiro (Eds.), Iron-Sulfur Proteins, Advances in Inorganic Chemistry, vol. 38, Academic Press, London, 1992.
[20] R. Cammack, T.G. Spiro (Eds.), Iron–Sulfur Proteins, Advances in Inorganic Chemistry, vol. 47, Academic Press, San Diego, CA, 1999.
[21] C.D. Stout, in: T.G. Spiro (Ed.), Iron–Sulfur Proteins, Metal Ions in Biology, Wiley, New York, 1982, pp. 97–146.
[22] W.R. Dunham, A.J. Bearden, I.T. Salmeen, G. Palmer, R.H. Sands, W.H. Orme-Johnson, H. Beinert, Biochim. Biophys. Acta 253 (1971) 134.
[23] W.R. Dunham, G. Palmer, R.H. Sands, A.J. Bearden, Biochim. Biophys. Acta 253 (1971) 373.
[24] L. Petersson, R. Cammack, K.K. Rao, Biochim. Biophys. Acta 622 (1980) 18.
[25] P. Bertrand, J.-P. Gayda, Biochim. Biophys. Acta 680 (1982) 331.
[26] L. Noodleman, E.J. Baerends, J. Am. Chem. Soc. 106 (1984) 2316.

[27] G. Blondin, J.J. Girerd, Chem. Rev. 90 (1990) 1359.
[28] V. Papaefthymiou, J.J. Girerd, I. Moura, J.J.G. Moura, E. Munck, J. Am. Chem. Soc. 109 (1987) 4703.
[29] E.L. Bominaar, Z.G. Hu, E. Munck, J.J. Girerd, S.A. Borshch, J. Am. Chem. Soc. 117 (1995) 6976.
[30] S.K. Chapman, S. Daff, A.W. Munro, Sruct. Bond. 88 (1997) 39.
[31] G. Palmer, in: A.B.P. Lever, H.B. Gray (Eds.), Iron Porphyrins, Part II, Addison-Wesley, London, 1983, p. 43.
[32] M.W. Makinen, A.K. Churg, in: A.B.P. Lever, H.B. Gray (Eds.), Iron Porphyrins, Part I, Physical Bioinorganic Chemistry Series, Addison-Wesley, London, 1983, pp. 141–236.
[33] P.G. Debrunner, in: A.B.P. Lever, H.B. Gray (Eds.), Iron Porphyrins, Part III, VCH, New York, 1989, p. 137.
[34] L.J. Marnett, T.A. Kennedy, in: P.R. Ortiz de Montellano (Ed.), Cytochrome P450: Structure, Mechanism, and Biochemistry, 2nd edition, Plenum, New York, 1995, pp. 49–83.
[35] A.X. Trautwein, E. Bill, E.L. Bominaar, H. Winkler, Struct. Bond. 78 (1991) 1.
[36] G. Loew, in: E.I. Solomon, A.B.P. Lever II (Eds.), Inorganic Electronic Structure and Spectroscopy, vol. II, Wiley, New York, 1999, pp. 451–531.
[37] P.J. Stephens, D.R. Jollie, A. Warshel, Chem. Rev. 96 (1996) 2491.
[38] R.H. Holm, P. Kennepohl, E.I. Solomon, Chem. Rev. 96 (1996) 2239.
[39] M.V. Botuyan, A. Toy-Palmer, J. Chung, R.C. Blake II, P. Beroza, D.A. Case, J.H. Dyson, J. Mol. Biol. 263 (1996) 752.
[40] H.-X. Zhou, J. Biol. Inorg. Chem. 2 (1997) 109.
[41] I. Bertini, G. Gori-Savellini, C. Luchinat, J. Biol. Inorg. Chem. 2 (1997) 114.
[42] A.G. Mauk, G.R. More, J. Biol. Inorg. Chem. 2 (1997) 119.
[43] M.R. Gunner, E. Alexov, E. Torres, S. Lipovaca, J. Biol. Inorg. Chem. 2 (1997) 126.
[44] G. Náray-Szabó, J. Biol. Inorg. Chem. 2 (1997) 135.
[45] F.A. Armstrong, J. Biol. Inorg. Chem. 2 (1997) 139.
[46] A. Warshel, A. Papazyan, I. Muegge, J. Biol. Inorg. Chem. 2 (1997) 143.
[47] R.A. Marcus, N. Sutin, Biochim. Biophys. Acta 811 (1985) 265.
[48] M.D. Lowery, J.A. Guckert, M.S. Gebhard, E.I. Solomon, J. Am. Chem. Soc. 115 (1993) 3012.
[49] E.I. Solomon, M.D. Lowery, Science 259 (1993) 1575.
[50] E.I. Solomon, K.W. Penfield, A.A. Gewirth, M.D. Lowery, S.E. Shadle, J.A. Guckert, L.B. Lacroix, Inorg. Chim. Acta 243 (1996) 67.
[51] P.M.H. Kroneck, W.E. Antholine, D.H.W. Kastrau, G. Buse, G.C.M. Steffens, W.G. Zumft, FEBS Lett. 268 (1990) 274.
[52] D.R. Gamelin, D.W. Randall, M.T. Hay, R.P. Houser, T.C. Mulder, G.W. Canters, S. Devries, W.B. Tolman, Y. Lu, E.I. Solomon, J. Am. Chem. Soc. 120 (1998) 5246.
[53] J.A. Farrar, F. Neese, P. Lappalainen, P.M.H. Kroneck, M. Saraste, W.G. Zumft, A.J. Thomson, J. Am. Chem. Soc. 118 (1996) 11501.
[54] J.C. Deaton, M.S. Gebhard, E.I. Solomon, Inorg. Chem. 28 (1989) 877.
[55] J.S. Griffith, The Theory of Transition-Metal Ions, University Press, Cambridge, 1964.
[56] N.V. Shokhirev, F.A. Walker, J. Am. Chem. Soc. 120 (1998) 981.
[57] C.P.S. Taylor, Biochim. Biophys. Acta 491 (1977) 137.
[58] G.H. Loew, in: A.B.P. Lever, H.B. Gray (Eds.), Iron Porphyrins, Part I, Physical Bioinorganic Chemistry Series, Addison-Wesley, London, 1983, pp. 1–88.
[59] R.J.P. Williams, Eur. J. Biochem. 234 (1995) 363.
[60] B.G. Malmström, Eur. J. Biochem. 223 (1994) 711.
[61] The words 'entatic' (as used by Williams [59]) and 'rack-induced' (as used by Malmström [60]) both describe a rigid protein enforcing a 'unique' ligation environment upon the metal active site relative to small molecule complexes. In the case of blue copper proteins this has been described as the protein imposing a Cu(I)-preferred geometry on a Cu(II) oxidation state. According to Williams [59], the original Lumry and Eyring [62] description of the effect of the protein matrix upon the metal center allowed for two possible modes of 'energization' — a rigid matrix concept versus an allosteric interaction involving a global shift in the protein matrix. The former

corresponds to what Williams calls an entatic state, while the latter is referred to as a rack-induced state by Lumry and Eyring (and Williams).
[62] R. Lumry, H. Eyring, J. Phys. Chem. 58 (1954) 110.
[63] J.M. Guss, H.D. Bartunik, H.C. Freeman, Acta Crystallogr. Sect. B 48 (1992) 790.
[64] E.I. Solomon, J.W. Hare, H.B. Gray, Proc. Natl. Acad. Sci. USA. 73 (1976) 1389.
[65] B.G. Malmström, T. Vänngård, J. Mol. Biol. 2 (1960) 118.
[66] J.L. Hughey IV, T.G. Fawcett, S.M. Rudich, R.A. Lalancette, J.A. Potenza, H.J. Shugar, J. Am. Chem. Soc. 101 (1979) 2617.
[67] K.W. Penfield, A.A. Gewirth, E.I. Solomon, J. Am. Chem. Soc. 107 (1985) 4519.
[68] A.A. Gewirth, E.I. Solomon, J. Am. Chem. Soc. 110 (1988) 3811.
[69] L.B. LaCroix, S.E. Shadle, Y.N. Wang, B.A. Averill, B. Hedman, K.O. Hodgson, E.I. Solomon, J. Am. Chem. Soc. 118 (1996) 7755.
[70] S. Larsson, A. Broo, L. Sjolin, J. Phys. Chem. 99 (1995) 4860.
[71] K. Pierloot, J.O.A. Dekerpel, U. Ryde, B.O. Roos, J. Am. Chem. Soc. 119 (1997) 218.
[72] B. Hedman, K.O. Hodgson, E.I. Solomon, J. Am. Chem. Soc. 112 (1990) 1643.
[73] S.E. Shadle, J.E. Penner-Hahn, H.J. Schugar, B. Hedman, K.O. Hodgson, E.I. Solomon, J. Am. Chem. Soc. 115 (1993) 767.
[74] S.J. George, M.D. Lowery, E.I. Solomon, S.P. Cramer, J. Am. Chem. Soc. 115 (1993) 2968.
[75] M.D. Newton, J. Phys. Chem. 92 (1988) 3049.
[76] M.D. Newton, Chem. Rev. 91 (1991) 767.
[77] D.N. Beratan, J.N. Betts, J.N. Onuchic, Science 252 (1991) 1285.
[78] S.S. Skourtis, J.J. Regan, J.N. Onuchic, J. Phys. Chem. 98 (1994) 3379.
[79] H.B. Gray, J.R. Winker, Annu. Rev. Biochem. 65 (1996) 537.
[80] C.C. Moser, J.M. Keske, K. Warncke, R.S. Farid, P.L. Dutton, Nature 355 (1992) 796.
[81] H.M. McConnel, J. Chem. Phys. 35 (1961) 508.
[82] J.A. Guckert, M.D. Lowery, E.I. Solomon, J. Am. Chem. Soc. 117 (1995) 2817.
[83] F.H. Allen, O. Kennard, Chem. Des. Autom. News 8 (1993) 31.
[84] A.L.E. Stoffels, W.G. Haanstra, W.L. Driessen, J. Reedijk, Angew. Chem. Int. Ed. Engl. 29 (1990) 1419.
[85] Anticipating the trigonal distortion of the tetrahedral geometry, the d orbitals in Fig. 6 are labeled where the three-fold axis is *z*.
[86] Due to spin-orbit coupling the LT-MCD C-term intensity is much larger for LF transitions than for CT transitions which allows their assignment.
[87] L.B. LaCroix, D.W. Randall, A.M. Nersissian, C.W.G. Hoitink, G.W. Canters, J.S. Valentine, E.I. Solomon, J. Am. Chem. Soc. 120 (1998) 9621.
[88] D.W. Randall, D.R. Gamelin, L.B. LaCroix, E.I. Solomon, J. Biol. Inorg. Chem. 5 (2000) 16.
[89] V.T. Aikazyan, R.M. Nalbandyan, FEBS Lett. 55 (1975) 272.
[90] T. Sakurai, H. Okamoto, K. Kawahara, A. Nakahara, FEBS Lett. 147 (1982) 220.
[91] J. Peisach, W.G. Levine, W.E. Blumberg, J. Biol. Chem. 242 (1967) 2847.
[92] B.G. Malmström, B. Reinhammar, T. Vänngård, Biochim. Biophys. Acta 205 (1970) 48.
[93] P.J. Hart, A.M. Nesissian, R.G. Herrmann, R.M. Nalbandyan, J.S. Valentine, D. Eisenberg, Protein Sci. 5 (1996) 2175.
[94] A. Romero, C.W.G. Hoitink, H. Nar, R. Huber, A. Messerschmidt, G.W. Canters, J. Mol. Biol. 229 (1993) 1007.
[95] K. Pierloot, J.O.A. Dekerpel, U. Ryde, M.H.M. Olsson, B.O. Roos, J. Am. Chem. Soc. 120 (1998) 13156.
[96] C.R. Andrew, H. Yeom, J.S. Valentine, B.G. Karlsson, N. Bonander, G. van Pouderoyen, G.W. Canters, T.M. Loehr, J. Sanders-Loehr, J. Am. Chem. Soc. 116 (1994) 11489.
[97] C.R. Andrew, J. Sanders-Loehr, Acc. Chem. Res. 29 (1996) 365.
[98] E.T. Adman, J.W. Godden, S. Turley, J. Biol. Chem. 270 (1995) 27458.
[99] J.M. Guss, E.A. Merritt, R.P. Phizackerley, H.C. Freeman, J. Mol. Biol. 259 (1996) 686.
[100] J. Han, T.M. Loehr, Y. Lu, J.S. Valentine, B.A. Averill, J. Sanders-Loehr, J. Am. Chem. Soc. 115 (1993) 4256.
[101] T. Sakurai, S. Sawada, A. Nakahara, Inorg. Chim. Acta 123 (1986) L21.

[102] There is a recent suggestion that in N_2OR the Cu center associated with the Cu_A spectral features (a $Cu^{1.5+}Cu^{1.5+}$ oxidation state) can be further oxidized to a Cu(II)Cu(II) state [103]
[103] J.A. Farrar, W.G. Zumft, A.J. Thomson, Proc. Natl. Acad. Sci. USA 95 (1998) 9891.
[104] S. Ferguson-Miller, G.T. Babcock, Chem. Rev. 96 (1996) 2889.
[105] B.E. Ramirez, B.G. Malmström, J.R. Winkler, H.B. Gray, Proc. Natl. Acad. Sci. USA 92 (1995) 11949.
[106] W.G. Zumft, P.M.H. Kroneck, in: R.P. Hausinger, G.L. Eichhorn, L.G. Marzilli (Eds.), Advances in Inorganic Biochemistry: Mechanisms of Metallocenter Assembly, vol. 11, VCH, New York, 1996, pp. 193–221.
[107] J.A. Farrar, A.J. Thomson, M.R. Cheesman, D.M. Dooley, W.G. Zumft, FEBS Lett. 294 (1991) 11.
[108] P.J. Hay, J.C. Thibeault, R. Hoffmann, J. Am. Chem. Soc. 97 (1975) 4884.
[109] D.R. Gamelin, E.L. Bominaar, M.L. Kirk, K. Wieghardt, E.I. Solomon, J. Am. Chem. Soc. 118 (1996) 8085.
[110] D.R. Gamelin, E.L. Bominaar, C. Mathoniere, M.L. Kirk, K. Wieghardth, J.J. Girerd, E.I. Solomon, Inorg. Chem. 35 (1996) 4323.
[111] We describe the electronic interactions between two metal ions in a cluster using H_{AB}, while the electronic coupling between two redox centers through bridging (protein) ligand is designated by H_{DA}. H_{AB} can have both direct metal orbital overlap and bridging ligand contributions called superexchange, while H_{DA} involves only electronic coupling through the bridging protein and therefore only involves superexchange. The electronic coupling within a cluster is much stronger than between redox centers: H_{AB} is typically on the order of 10 000 cm^{-1}, while H_{DA} is typically on the order of 1 cm^{-1}.
[112] A. Cramer, Physica 1 (1934) 191.
[113] C. von Wachenfeldt, S. de Vries, J. van der Oost, FEBS Lett. 340 (1994) 109.
[114] M. Hay, J. Richards, Y. Lu, Proc. Natl. Acad. Sci. USA 93 (1996) 461.
[115] C. Dennison, E. Vijgenboom, S. de Vries, J. van der Oost, G.W. Canters, FEBS Lett. 365 (1995) 92.
[116] R.P. Houser, V.G. Young Jr., W.B. Tolman, J. Am. Chem. Soc. 118 (1996) 2101.
[117] R.P. Houser, J.A. Halfen, V.G. Young Jr., N.J. Blackburn, W.B. Tolman, J. Am. Chem. Soc. 117 (1996) 10745.
[118] S.E. Wallace-Williams, C.A. James, S. de Vries, M. Saraste, P. Lappalainen, J. van der Oost, M. Fabian, G. Palmer, W.H. Woodruff, J. Am. Chem. Soc. 118 (1996) 3986.
[119] C.R. Andrew, R. Fraczkiewicz, R.S. Czernuszewicz, P. Lappalainen, M. Saraste, J. Sanders-Loehr, J. Am. Chem. Soc. 118 (1996) 10436.
[120] K.R. Williams, D.R. Gamelin, L.B. LaCroix, R.P. Houser, W.B. Tolman, T.C. Mulder, S. DeVries, B. Hedman, K.O. Hodgson, E.I. Solomon, J. Am. Chem. Soc. 119 (1997) 613.
[121] The preliminary estimate of the covalency (26% total S character) [120] in the Cu_A site is in fact an underestimate [122] and the quantitization is consistent with the higher covalency from EPR studies [123,124].
[122] S. DeBeer, D.W. Randall, Y. Lu, W.B. Tolman, B. Hedman, K.O. Hodgson, E.I. Solomon (2000) in preparation.
[123] F. Neese, W.G. Zumft, W.E. Antholine, P.M.H. Kroneck, J. Am. Chem. Soc. 118 (1996) 8692.
[124] F. Neese, R. Kappl, W.G. Zumft, J. Hüttermann, P.M.H. Kroneck, J. Biol. Inorg. Chem. 3 (1998) 53.
[125] S.B. Piepho, E.R. Krausz, P.N. Schatz, J. Am. Chem. Soc. 100 (1978) 2996.
[126] With the monomeric breathing modes Q_A and Q_B, the Q_- mode is $2^{-1/2}(Q_A - Q_B)$ [27,125]. The dimensionless coordinate x_- is along the Q_- mode, $x_- = Q_-/(\Lambda/k_-)$, where $k_- = 4\pi^2 c^2 \mu_- \nu_-^2$ in which ν_- and μ_- are the frequency and modal mass of the Q_- mode, respectively [27,125]. The quantity Λ is the vibronic coupling parameter where $\Lambda^2/k_- \approx k_-[n^{1/2}\Delta r_{redox}]^2$, in which n is the number of metal–ligand bond length changes and Δr_{redox} is the difference in metal–ligand bond lengths between the oxidized and reduced structures.
[127] M.T. Hay, M.C. Ang, D.R. Gamelin, E.I. Solomon, W.E. Antholine, M. Ralle, N.J. Blackburn, P.D. Massey, X.T. Wang, A.H. Kwon, Y. Lu, Inorg. Chem. 37 (1998) 191.

[128] J.J. Regan, B.E. Ramirez, J.R. Winkler, H.B. Gray, B.G. Malmström, J. Bioenerg. Biomembr. 30 (1998) 35.
[129] R.J. Gurbiel, Y.C. Fann, K.K. Surerus, M.M. Werst, S.M. Musser, P.E. Doan, S.I. Chan, J.A. Fee, B.M. Hoffman, J. Am. Chem. Soc. 115 (1993) 10888.
[130] H. Witt, F. Malatesta, F. Nicoletti, M. Brunori, B. Ludwig, J. Biol. Chem. 273 (1998) 5132.
[131] H. Robinson, M.C. Ang, Y.-G. Gao, M.T. Hay, Y. Lu, A.H.-J. Wang, Biochemistry 38 (1999) 5677.
[132] When compared to literature values for $\sigma-\sigma^*$ transition energies for first row transition metal dimers with unsupported (i.e. no ligand contributions to $\sigma-\sigma^*$ splitting) metal–metal bonds ($E_{\sigma-\sigma^*} > 24\,000$ cm^{-1}), [133] the analogous bond in Cu_A is rather weak, as the metal–metal contribution to $E^{-}_{\sigma-\sigma^*}$ is only 7800 cm^{-1}.
[133] H.B. Abrahamson, C.C. Frazier, D.S. Ginley, H.B. Gray, J. Lilienthal, D.R. Tyler, M.S. Wrighton, Inorg. Chem. 16 (1977) 1554.
[134] S. Drueke, P. Chaudhuri, K. Pohl, K. Wieghardt, X.Q. Ding, E. Bill, A. Sawaryn, A.X. Trautwein, H. Winkler, S.J. Gurman, J. Chem. Soc. Chem. Commun. (1989) 59.
[135] X.Q. Ding, E.L. Bominaar, E. Bill, H. Winkler, A.X. Trautwein, S. Drueke, P. Chaudhuri, K. Wieghardt, J. Chem. Phys. 92 (1990) 178.
[136] X.Q. Ding, E.L. Bominaar, E. Bill, H. Winkler, A.X. Trautwein, S. Drueke, P.H. Chaudhuri, K. Wieghardt, Hyperfine Interact. 53 (1990) 311.
[137] G. Peng, J. van Elp, H. Jang, L. Que, W.H. Armstrong, S.P. Cramer, J. Am. Chem. Soc. 117 (1995) 2515.
[138] P.N. Schatz, in: E.I. Solomon, A.B.P. Lever (Eds.), Inorganic Electronic Structure and Spectroscopy, vol. II, Wiley, New York, 1999, pp. 175–226.
[139] C. Creutz, H. Taube, J. Am. Chem. Soc. 91 (1969) 3988.
[140] C. Creutz, H. Taube, J. Am. Chem. Soc. 95 (1973) 1086.
[141] C. Creutz, Prog. Inorg. Chem. 30 (1983) 1.
[142] E. Sinn, Coord. Chem. Rev. 5 (1970) 347.
[143] A.P. Ginsberg, Inorg. Chim. Acta Rev. 5 (1971) 45.
[144] J.S. Griffith, Struct. Bond. 10 (1972) 87.
[145] O. Kahn, Angew. Chem. 97 (1985) 837.
[146] O. Kahn, Molecular Magnetism, 1st edition, VCH, New York, 1993.
[147] C. Zener, Phys. Rev. 82 (1951) 403.
[148] P.W. Anderson, H. Hasegawa, Phys. Rev. 100 (1955) 675.
[149] J.-J. Girerd, J. Chem. Phys. 79 (1983) 1766.
[150] V. Papaefthymou, J.-J. Girerd, I. Moura, J.J.G. Moura, E. Münck, J. Am. Chem. Soc. 109 (1987) 4703.
[151] E. Münck, V. Papaefthymiou, K.K. Surerus, J.-J. Girerd, in: E. Münck, V. Papaefthymiou, K.K. Surerus, J.-J. Girerd (Eds.), Double Exchange in Reduced Fe_3S_4 Clusters and Novel Clusters with MFe_3S_4 Cores, vol. 372, American Chemistry Society, Washington, DC, 1988.
[152] J.J. Girerd, V. Papaefthymiou, K.K. Surerus, E. Munck, Pure Appl. Chem. 61 (1989) 805.
[153] G. Blondin, S. Borshch, J.-J. Girerd, Comments Inorg. Chem. 12 (1992) 315.
[154] M.I. Belinskii, Mol. Phys. 60 (1987) 793.
[155] S.A. Borshch, L.F. Chibotaru, Chem. Phys. 135 (1989) 375.
[156] If one uses an exponential model to estimate between 2.51 and 2.89 Å in Fig. 23 a similar B value of ca. 912 cm^{-1} is obtained for the 2.73 Å Fe–Fe distance of $[2Fe–2S]^+$.
[157] G. Palmer, in: W. Lovenberg (Ed.), Iron–Sulfur Proteins, vol. III, Academic Press, New York, 1973, pp. 285–325.
[158] Note that the inclusion of vibronic coupling changes the energy splittings as can be seen in Fig. 26 and leads to a small change in the value of J relative to that estimated with the inclusion of only HDvV coupling and double exchange.
[159] E. Münck, T.A. Kent, Hyperfine Interact. 27 (1980) 161.
[160] S.A. Borshch, E.L. Bominaar, G. Blondin, J.-J. Girerd, J. Am. Chem. Soc. 115 (1993) 5155.
[161] C.W. Carter Jr., J. Kraut, S.T. Freer, R.A. Alden, L.C. Sieker, E. Adman, L.H. Jensen, Proc. Natl. Acad. Sci. USA 69 (1972) 3526.

[162] L. Noodleman, Inorg. Chem. 30 (1991) 246.
[163] L. Noodleman, Inorg. Chem. 30 (1991) 256.
[164] I. Bertini, F. Briganti, C. Luchinat, A. Scozzafava, M. Sola, J. Am. Chem. Soc. 113 (1991) 1237.
[165] S.A. Borshch, E.L. Bominaar, J.J. Girerd, New J. Chem. 17 (1993) 39.
[166] E.L. Bominaar, S.A. Borshch, J.J. Girerd, J. Am. Chem. Soc. 116 (1994) 5362.
[167] Neither the trinuclear nor tetranuclear cluster shows complete delocalization of the excess electron over all of the iron centers.
[168] S.E. Shadle, B. Hedman, K.O. Hodgson, E.I. Solomon, Inorg. Chem. 33 (1994) 4235.
[169] S.E. Shadle, B. Hedman, K.O. Hodgson, E.I. Solomon, J. Am. Chem. Soc. 117 (1995) 2259.
[170] K.R. Williams, B. Hedman, K.O. Hodgson, E.I. Solomon, Inorg. Chim. Acta 263 (1997) 315.
[171] K. Rose, S.E. Shadle, M.K. Eidsness, D.M. Kurtz, R.A. Scott, B. Hedman, K.O. Hodgson, E.I. Solomon, J. Am. Chem. Soc. 120 (1998) 10743.
[172] K. Rose, E.S. Shadle, T. Glaser, S.D. Vries, A. Cherepanow, G.W. Canters, B. Hedman, K.O. Hodgson, E.I. Solomon, J. Am. Chem. Soc. 121 (1999) 2353.
[173] Y. Izumi, T. Glaser, K. Rose, J. McMaster, P. Basu, J.H. Enemark, B. Hedman, K.O. Hodgson, E.I. Solomon, J. Am. Chem. Soc. 121 (1999) 10035.
[174] T. Glaser, K. Rose, S.E. Shadle, B. Hedman, K.O. Hodgson, E.I. Solomon, in preparation.
[175] T. Glaser, B. Hedman, K.O. Hodgson, E.I. Solomon, Acc. Chem. Res., submitted for publication.
[176] M. Nishi, Y. Ito, A. Ito, J. Phys. Chem. Jpn. 52 (1983) 3602.
[177] J.M. Mouesca, J.L. Chen, L. Noodleman, D. Bashford, D.A. Case, J. Am. Chem. Soc. 116 (1994) 11898.